Greenland Monthly Accumulation Maps (1960-2022): A Statistical Semi-Empirical Bias-Adjustment Model

Josephine Lindsey-Clark[1], Aslak Grinsted[1], Baptiste Vandecrux[2], and Christine Schøtt Hvidberg[1]

[1]Physics of Ice, Climate, and Earth, Niels Bohr Institute, University of Copenhagen, Jagtvej 132, 2200 Copenhagen, Denmark
[2]Geological Survey of Denmark and Greenland, Øster Voldgade 10, 1350 Copenhagen, Denmark

Correspondence: Josephine Lindsey-Clark (josephine.lindsey-clark@nbi.ku.dk)

Abstract.

Accurate estimates of snow accumulation over the Greenland ice-sheet are essential for reliable projections of sea-level rise. These are typically obtained from regional climate models, which carry systematic temporal and spatially variable biases, contributing to substantial uncertainties in sea-level rise projections. Here we present a novel statistical-semi-empirical model for bias-correcting gridded accumulation output from any regional climate model or reanalysis product, utilising the SUMup dataset, which provides the most comprehensive spatial and temporal coverage of surface mass balance observations to date. The method employs Empirical Orthogonal Function analysis to decompose the model accumulation output into the dominant patterns of spatial variability and their temporal evolution. Adjustment coefficients derived by fitting SUMup data enable the reconstruction of spatially complete, bias-corrected accumulation fields.

We apply this approach to monthly accumulation output from the HIRLAM–ECHAM Regional Climate Model (HIRHAM5; 1960–2022), the Modèle Atmosphérique Régional (MAR3.14; 1960–2022), the Regional Atmospheric Climate Model (RACMO 2.4p1; 1980–2022), and the Copernicus Arctic Regional Reanalysis (CARRA; 1991–2022). Initial mean point-wise biases of -7.4% (HIRHAM), -0.5% (MAR), 0.0% (RACMO) and +10.1% (CARRA) (1991-2022), statistically significant for all models except RACMO, are reduced to ±0.3% following adjustment. Resulting bias-corrected mean annual accumulation rates over the ice sheet are estimated at 469 mm yr^{-1} (HIRHAM), 412 mm yr^{-1} (MAR), 435 mm yr^{-1} (RACMO) and 408 mm yr^{-1} (CARRA) between 1991-2022. Inter-model agreement improves significantly in the observation-rich accumulation zone, with a 68% reduction in standard deviation of mean accumulation estimates, but deteriorates by 27% in the sparsely sampled ablation zone, highlighting the need for additional observational constraints. Model bias is dominated by the southern ice sheet, with the largest statistically significant contributions from the south-east for HIRHAM (-39 to -54 Gt yr^{-1}) and MAR (+30 to +33 Gt yr^{-1}), and the south-west for RACMO (+20 to +26 Gt yr^{-1}) and CARRA (+34 Gt yr^{-1}). Temporal trends and temperature sensitivities exhibit a pronounced east-west contrast, with the east dominated by strong positive responses and negative responses in the west.

The framework outlined in this study offers a scalable, transferable solution to improve accumulation estimates through enhanced integration of observational data, providing an improved input to ice-sheet models, with the potential to reduce uncertainties in future sea-level rise projections.

1 Introduction

The Greenland Ice Sheet (GrIS) has become the greatest single cryospheric contributor to present-day global sea-level rise (Chen et al., 2017; van den Broeke et al., 2017, 2016), accounting for approximately 22% of the $\sim$3.3 mm yr^{-1} total mean sea-level rise between 2002 to 2022 (Hanna et al., 2024; Jia et al., 2022). Since the mid 1990s, mass loss from the GrIS has been driven by changes in Surface Mass Balance (SMB) (Hofer et al., 2020; van den Broeke et al., 2016, 2009), overtaking ice loss from calving. SMB is defined as the mass accumulated through precipitation, minus the mass lost through meltwater runoff, sublimation, evaporation, and wind redistribution. As the only net mass input, accumulation is crucial to constrain for accurate modelling of ice-sheet evolution. However, due to the complexity of the processes governing precipitation, coupled with limitations in model resolution and simplified cloud microphysics, accumulation over the GrIS remains poorly constrained by models. As a result, regional climate models (RCMs) often fail to adequately capture this variability, leading to biased estimations of ice mass loss (Ryan et al., 2020) and substantial discrepancies between climate model projections (Otosaka et al., 2023).

The first studies investigating snow accumulation began in the early 20th century, establishing techniques such as stake measurements, snow pits, and shallow cores to deduce accumulation from snow height and seasonal layering. Ice core projects starting in the late 1950s analysing stable oxygen-isotope ratios provided new insights into past climate, later leading to the systematic use of ice cores for detailed accumulation studies (e.g. Box et al., 2013, 2009; Buchardt et al., 2012; Mosley-Thompson et al., 2001; Clausen et al., 1988). The introduction of ice-penetrating radar systems in the mid-1960s to track reflections from internal ice layers revealed that stratified ice layers formed by seasonal snowfall could be used to infer accumulation rates. Unlike ice cores, snow pits and stake measurements, which provided point observations, radar techniques enabled continuous mapping over vast regions. Early radar studies, such as (Robin et al., 1969), demonstrated the effectiveness of radar in revealing accumulation variability over broad regions, laying the foundation for further ground-based radar surveys (Hawley et al., 2014; Miège et al., 2013; Medley et al., 2013), as well as airborne campaigns (Montgomery et al., 2020; Lewis et al., 2017; Koenig et al., 2016). These advances allowed for systematic coverage of regions of the ice sheet that were previously inaccessible to in situ measurements, dramatically improving our understanding of accumulation patterns.

One of the earliest comprehensive efforts to synthesise a diverse range of observational data to map accumulation across the GrIS was by Ohmura and Reeh (1991). Using spatial interpolation of measurements from snow pits, ice cores and coastal weather stations, they estimated the mean accumulation to be 310 mm.w.e, and provided one of the most accurate maps of accumulation over the ice sheet at the time. This influential study played a crucial role in improving understanding of how topography and weather systems influence regional snowfall patterns and ice sheet mass balance. Subsequent studies incorporated additional data with improved interpolation techniques (Cogley, 2004; Calanca et al., 2000; Ohmura et al., 1999), and enhanced understanding of regional variability (McConnell et al., 2001).

Regional climate models provided a way to estimate accumulation patterns on a spatially complete, high resolution grid (Ettema et al., 2009; Fettweis et al., 2008; Box et al., 2006; Box, 2005; Box et al., 2004). Similarly, climate reanalysis data were used to provide accumulation grids (Hanna et al., 2008, 2006, 2005), with the advantage of assimilating remotely-sensed and in-situ observations, such as atmospheric measurements of pressure and temperature (Simmons and Gibson, 2000). Reanalysis datasets could also serve as boundary conditions for RCM simulations, alongside ancillary observational datasets such as those from weather stations and remote sensing. However, both RCMs and reanalysis products inherently carry biases arising from coarse spatial resolution failing to resolve complex terrain, simplified cloud microphysics schemes, and sparse observational constraints.

To address model bias, Box et al. (2006) calibrated accumulation output from the Fifth Generation Mesoscale Model for polar climates (Polar MM5) using snow pit observations, identifying and correcting for systematic errors. Expanding on these advances, Burgess et al. (2010) combined firn core measurements and meteorological station precipitation data with high-resolution Polar MM5 output to create a spatially complete reconstruction of Greenland Ice Sheet accumulation. This hybrid methodology resolved inconsistencies in earlier studies that relied on sparse datasets or models alone, providing a new accumulation grid with enhanced regional accuracy. Using spatial interpolation of linear correction functions derived by region, Burgess found a mean snow accumulation rate of 337 ± 48 mm yr^{-1} w.e, 16-21% higher than previous estimates by Ohmura et al. (1999), Calanca et al. (2000) and Cogley (2004). This increase was primarily attributed to better representation of higher orographic precipitation provided by the hybrid approach, affecting the south-east in particular—a region with limited ice core coverage. Accumulation rates in the south-east were found to exceed 2000 mm yr^{-1} and dominate the inter-annual variability. Representing 31% of the total accumulated mass, this region was found to have a substantial impact on the ice-sheet surface mass balance as a whole.

Providing one of the first spatially complete reconstructions of accumulation, Burgess et al. (2010) remains a cornerstone for understanding Greenland's climate-driven ice loss. Since then, numerous studies have continued to improve on this foundation through incorporating new observational data and enhanced model simulations (Mouginot et al., 2019; Sandberg Sørensen et al., 2018; van den Broeke et al., 2016; Khan et al., 2015; Velicogna et al., 2014; Box et al., 2013; Shepherd et al., 2012). Despite these advances, accumulation remains a major source of uncertainty in projections of future sea-level rise (van den Broeke et al., 2009).

Ice sheet models, and thus sea-level rise projections, require spatially complete gridded accumulation maps and are therefore typically obtained from RCMs. RCMs are often validated using a combination of remote sensing data and in-situ point observations from weather stations and firn cores. Although remote sensing technology can provide snowfall estimates, the accuracy of retrievals is restricted by challenges in sampling limitations and ground clutter (Ryan et al., 2020; Bennartz et al., 2019). Combined with the sparse distribution of weather stations and firn cores leaving vast regions without in-situ coverage, RCM accumulation maps still carry significant uncertainties today (Ryan et al., 2020; Vernon et al., 2013). Though in situ accumulation data from ice cores, radar, snow pits and stake measurements can fill some in-situ data gaps, uncertainties introduced by point-to-pixel differences, coupled with challenges in aligning the inconsistent temporal resolutions, means that the full range of available data has remained under-utilised in systematic RCM validation.

Here we present a flexible statistical-semi-empirical model designed to utilise the full range of available in-situ data to bias-adjust any gridded model accumulation output. This study advances prior work through leveraging the SUMup surface mass balance dataset (Vandecrux et al., 2024), providing the most comprehensive basis for model correction to date. Using this diverse compilation of in-situ data derived primarily from ice-cores, airborne and ground-based radar, snow pits, stake measurements and automated weather stations, we produce a data cube of monthly bias-adjusted spatially complete accumulation maps. While previous studies have used techniques such as universal kriging (Ohmura and Reeh, 1991), triangulated irregular networks (Burgess et al., 2010) and least-squares regressions (Box et al., 2013) to estimate or correct model fields with point-based observations, these approaches typically do not explicitly account for patterns of both spatial and temporal bias variability.

We base our method on Empirical Orthogonal Function (EOF) decomposition of the model accumulation output, which reveals the dominant patterns of spatial and temporal variability. Utilising robust least-squares optimisation, we fit each component of the decomposition to SUMup observations to derive a set of coefficients which adjust each component of the decomposition. This approach enables targeted correction of the model's spatial and temporal structure.

The aim of this study is to present a flexible bias-correction model for improving estimates of GrIS accumulation, which offers the potential to improve GrIS SMB estimates and downstream modelling of sea-level rise. We first present four model products to which the bias-adjustment is applied: the HIRLAM–ECHAM Regional Climate Model (HIRHAM) version 5, the Modèle Atmosphérique Régional (MAR) version 3.14, the Polar Regional Atmospheric Climate Model (RACMO) version 2.4p1, and the Copernicus Arctic Regional Reanalysis (CARRA), followed by an overview of the SUMup dataset and key data considerations. We then provide a detailed outline of the bias-adjustment method. Results are subsequently analysed in terms of mean and seasonal biases before and after bias-adjustment, and we examine the impact on long-term accumulation trends and temperature sensitivity. Lastly, we discuss the implications and limitations of these findings.

2 Data

2.1 Gridded Model Accumulation

We present bias-corrected accumulation maps for four models, including three RCMs and one reanalysis dataset: (1) the HIRLAM–ECHAM Regional Climate Model (HIRHAM) version 5 (Langen et al., 2017), (2) the Modèle Atmosphérique Régional (MAR) version 3.14 (Fettweis et al., 2020), (3) the Polar Regional Atmospheric Climate Model (RACMO) version 2.4p1 (van Dalum et al., 2024), and (4) the Copernicus Arctic Regional Reanalysis (CARRA) dataset (Schyberg et al., 2020). All models are forced with ERA5 (Hersbach et al., 2020) at their lateral boundaries. As none of the models are coupled with an ice-sheet model, the ice extent and topography are fixed through the simulations. Output data is obtained at monthly temporal resolution, with accumulation approximated using SMB components excluding runoff. The implications of this approximation relative to SUMup observations are discussed in section 2.3.

2.1.1 HIRHAM5 Regional Climate Model (1960-2022, 5.5 km)

HIRHAM5 (DMI et al., 2017), is the fifth generation of the HIRHLAM-ECHAM regional atmospheric climate model, which combines the dynamics of the HIRLAM model (Undén et al., 2002) with the physical parametrisation schemes of the ECHAM model (Roeckner et al., 2003). Over the Greenland domain used here, HIRHAM5 is run on a horizontal rotated latitude–longitude grid with ∼5.5 km resolution, using 31 atmospheric levels and a time step of 90 s Langen et al. (2017). The model is 6-hourly forced at its lateral boundaries by ERA5 reanalysis (Hersbach et al., 2020) which provides atmospheric fields of temperature, humidity, wind and surface pressure. ERA5 sea surface temperatures and sea-ice concentrations are prescribed at the lower boundary. HIRHAM5 has been extensively evaluated against observations over Greenland (Langen et al., 2017, 2015; Lucas-Picher et al., 2012).

In HIRHAM, SMB is parametrised as:

$$SMB_{HIRHAM} = P - E - RU, \tag{1}$$

where P is the total precipitation, E, is evaporation including sublimation, and RU is surface meltwater runoff. Excluding runoff, we define accumulation as:

$$Acc_{HIRHAM} = P - E. \tag{2}$$

2.1.2 MARv3.14 Regional Climate Model (1960-2022, 5 km)

The Modèle Atmosphérique Régional (MAR) version 3.14 (Fettweis and Grailet, 2024) couples an atmospheric module Gallée and Schayes (1994) to Soil Ice Snow Vegetation Atmosphere Transfer (SISVAT) scheme (Ridder and Schayes, 1997), including a snow model based on CROCUS (Brun et al., 1992). The snow module resolves the dominant physical processes governing snowpack evolution, including thermal stratification, densification, meltwater percolation, grain size and snow drift. The model is forced at its lateral boundaries by ERA5 in 6-hour intervals, which also provides sea surface temperatures and sea ice cover over ocean grid cells (Haacker et al., 2024).

The model configuration has been calibrated over the GrIS (Fettweis et al., 2020) and extensively validated, showing improved agreement with in-situ atmospheric measurements (Delhasse et al., 2020), remote-sensing derived melt extent (Fettweis et al., 2011) and SMB observations (Fettweis et al., 2020), compared to earlier versions.

For MAR, SMB is parametrised as:

$$SMB_{MAR} = P - SU - SW - RU, \tag{3}$$

where P is total precipitation, SU is sublimation from snow/soil, SW is surface water and RU is surface meltwater runoff. Excluding runoff, accumulation is defined here as:

$$Acc_{MAR} = P - SU - SW. \tag{4}$$

2.1.3 RACMO2.4p1 Regional Climate Model (1980-2022, 11 km)

RACMO 2.4p1 (van Dalum et al., 2024), is a hydrostatic model that integrates the atmospheric dynamics of HIRLAM version 5.0.3 (Undén et al., 2002) with the physical parametrisations of the ECMWF Integrated Forecasting System. At the lateral boundaries, RACMO2.4p1 is forced by ERA5 reanalysis fields at 3-hourly intervals, including wind, temperature, humidity, and surface pressure, with sea surface temperature and sea-ice concentration also prescribed from ERA5. The polar version of RACMO includes specialised parameterisations for glaciated surfaces and polar boundary-layer processes, with a dedicated ice-sheet surface tile and a multilayer snow model that resolves snow metamorphism, compaction, melt, refreezing, and drifting-snow processes (Noël et al., 2018; Ettema et al., 2010). The simulations used here are taken from the R24 experiment on a pan-Arctic domain following the Arctic CORDEX standard, with a horizontal grid spacing of $\sim$11 km and 40 atmospheric layers.

RACMO2.4p1 shows generally good agreement with observations over Greenland, with improved representation of cloud microphysics, precipitation, and surface mass balance compared to the previous version (R23p3) (van Dalum et al., 2024).

In RACMO2.4p1, SMB is parametrised as:

$$SMB_{RACMO} = P - SU - ER - RU, \tag{5}$$

where P is precipitation, here SU is sublimation including surface sublimation and sublimation of wind blown snow, ER is drifting snow erosion and RU is surface meltwater runoff (van Dalum et al., 2024). Excluding runoff, we define accumulation as:

$$Acc_{RACMO} = P - SU - ER. \tag{6}$$

2.1.4 CARRA Reanalysis (1991-2022, 2.5 km)

The CARRA reanalysis dataset (Schyberg et al., 2020) is built on the weather forecast model HARMONIE, standing for HIRLAM–ALADIN Research on Mesoscale Operational NWP in Euromed, which integrates developments from HIRLAM (High Resolution Limited Area Model) and ALADIN (Aire Limitée Adaptation Dynamique Développement International) (Bengtsson et al., 2017). It is forced at its lateral boundaries by the ERA5 reanalysis (Hersbach et al., 2020) and applies three-dimensional variational (3D-Var) data assimilation to incorporate multiple datasets (Schyberg et al., 2020), including, in Greenland, remotely sensed surface albedo (Kokhanovsky et al., 2023) and temperature, humidity, and wind speed measured by on-ice weather stations (Fausto et al., 2021; Vandecrux et al., 2023). With 2.5 km horizontal resolution and an improved representation of cold surfaces (Yang et al., 2020), CARRA agrees substantially better with in situ observations than ERA5 (Køltzow et al., 2022). It has been used to investigate the recent warming over the Barents Sea (Isaksen et al., 2022), Arctic sea ice (Batrak et al., 2024) and increased glacier melt in Svalbard (Schmidt et al., 2023).

In CARRA, a dedicated SMB variable is not available, and we therefore define accumulation as:

$$Acc_{CARRA} = P - E - SU, \tag{7}$$

where P is the total precipitation, E is evaporation, and SU is the time integrated snow evaporation flux. Monthly data is obtained by subtracting the 30 hour and 6 hour daily forecasts and resampling to monthly sums.

2.2 Analysis Domain

We perform the bias-adjustment across the entire ice-sheet, defining a common ice mask derived from the PROMICE-2022 Ice Mask (Luetzenburg et al., 2025). This product provides a high-resolution delineation of the Greenland Ice Sheet and interior nunataks, encompassing a glacierised area of 1,725,648 km^2. Mapped from August 2022 Sentinel-2 imagery, it captures the GrIS margin with greater than 20 m horizontal accuracy, offering the most up-to-date and internally consistent representation of the GrIS extent currently available. Drainage basin boundaries used are also adopted from the PROMICE dataset.

We define the accumulation zone using the mask presented in (Vandecrux et al., 2019), which applies end-of-summer snow lines from Fausto et al. (2018) to identify the minimum firn area observed between 2000-2017. This region, covering 1,405,500 km^2, corresponds to the area where snow was persistent through the 2000-2017 period, with a boundary uncertainty of 1%, estimated by shifting the firn line by ± 1 km (Fausto et al., 2018). Within the PROMICE ice mask, this firn area represents $\sim$80% of the ice-sheet, with the remaining $\sim$20% classified here as the ablation zone (table 1).

Table 1. Ice-sheet area, accumulation and precipitation distribution across the full PROMICE ice mask (Ice sheet), the accumulation (Acc.) and ablation (Abl.) zones, shown for the 1991-2022 overlap period.

	Area [km^2]			**Accumulation** [Gt yr^{-1}]			**Precipitation** [Gt yr^{-1}]		
Model	Ice sheet	Acc. (%)	Abl. (%)	Ice sheet	Acc. (%)	Abl. (%)	Ice sheet	Acc. (%)	Abl. (%)
HIRHAM	1,803,373	1,412,429 (78%)	390,943 (22%)	805	528 (66%)	277 (34%)	837	533 (64%)	304 (36%)
MAR	1,803,203	1,415,090 (78%)	388,113 (22%)	779	572 (73%)	207 (27%)	836	597 (71%)	239 (29%)
RACMO	1,839,800	1,411,192 (77%)	428,608 (23%)	820	555 (68%)	265 (32%)	853	574 (67%)	278 (33%)
CARRA	1,790,894	1,424,244 (80%)	366,650 (20%)	808	607 (75%)	200 (25%)	883	643 (73%)	240 (27%)

2.3 SUMup In-Situ Observational Data

The SUMup collaborative database is a compilation of in situ measurements of SMB as well as subsurface temperature and density for the Greenland and Antarctic ice sheets from published and unpublished sources (Vandecrux et al., 2024). The 2024 edition contains, in a harmonised format, more than 2.4 million SMB values given between two dates or, if dates are unknown, between two years. Of these, over 2.1 million fall within the PROMICE ice mask, >95% of which lie within the accumulation zone (Fig. 1). The data are derived primarily from airborne radar (Montgomery et al., 2020; Lewis et al., 2017; Koenig et al., 2016), ground based radar (Lewis et al., 2019; Miège et al., 2013), ice/firn-cores (Kawakami et al., 2023; Freitag et al., 2022a, b, c; Vinther et al., 2022; Osman et al., 2021; Lewis et al., 2019; Graeter et al., 2018; Miege et al., 2014; Miège et al., 2013; Box et al., 2013; Hanna et al., 2011; Burgess et al., 2010; Bales et al., 2009; Banta and McConnell, 2007; Hanna et al., 2006; Mosley-Thompson et al., 2001; Miller and Schwager, 2000b, c, d, a; Hammer and Dahl-Jensen, 1999; Clausen et al., 1988), snow pits (Kjær et al., 2021; Niwano et al., 2020; Schaller et al., 2016; Bolzan and Strobel, 2001a, b, 1999a, b, c, d, e, f, g, 1994), stake measurements (Chandler et al., 2021, 2015; Hermann et al., 2018; Machguth et al., 2016; Dibb and Fahnestock, 2004), SnowFox sensors (Fausto, 2021) and estimated from mass balance profiles (Machguth et al., 2016). An overview of their spatial coverage by decade and season is provided in Appendix figures A1 and A2, respectively.

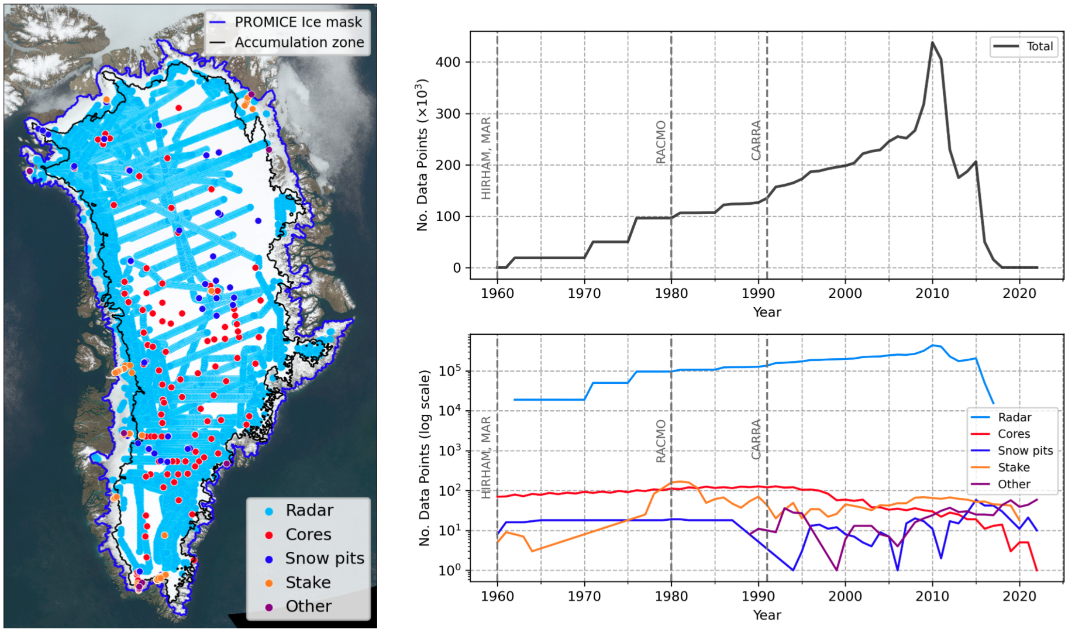

Figure 1. Left: geographical distribution of SUMup data points used in this study between 1960 and 2022, illustrated by measurement type. The method type ‘other’ includes mass balance profiles and SnowFox sensors. Right upper: time dependence of total number of data points with markers for the start year of model data. Right lower: time dependence of data points by measurement type, with counts in log scale.

To focus on constraining accumulation and not runoff, for which SUMup data are not sufficient, we filter out negative SMB observations in the ablation and percolation zones, thereby excluding measurements which may describe melt or runoff. This removes all data from automated weather stations, as well as a subset of those derived from stake measurements, SnowFox sensors records, and mass balance profiles. Any measurements that are substantially impacted by melt are already excluded in the SUMup release. Consequently, we consider the remaining observations to represent a reliable dataset for comparison with model accumulation output.

Most accumulation estimates in SUMup, particularly those derived from radar and ice cores, rely on density corrections to convert observed layer thicknesses into snow-water-equivalent values. This introduces additional uncertainty, especially where density profiles are sparse, inferred, or inconsistently applied. Prior to bias-adjustment, the SUMup data were inspected for potential issues, including inconsistencies resulting from processing or calculation errors. For example, we found discrepancies between the timestamps associated to accumulation values in Miège et al. (2013), the related dataset Miege et al. (2014) and those reported in the SUMup 2024 release. After testing alternative interpretations, pre-summer start and end dates were set to 1st January and 31st December, respectively, and post-summer start and end dates were set to 1st January the following year and 31st December, respectively. This interpretation was seen to improve the consistency with the rest of the dataset and model estimates.

Period	Model	Annual/multi-annual	Sub-annual	Monthly	Total
1960–2022	HIRHAM	98,181 (83.2%)	19,690 (16.7%)	191 (0.2%)	118,062
	MAR	97,296 (82.3%)	20,765 (17.6%)	191 (0.2%)	118,252
1980–2022	HIRHAM	82,779 (80.7%)	19,589 (19.1%)	191 (0.2%)	102,559
	MAR	82,423 (79.8%)	20,664 (20.0%)	191 (0.2%)	103,278
	RACMO	36,621 (80.1%)	8,888 (19.4%)	191 (0.4%)	45,700
1991–2022	HIRHAM	74,199 (79.1%)	19,402 (20.7%)	191 (0.2%)	93,792
	MAR	74,097 (78.2%)	20,477 (21.6%)	191 (0.2%)	94,765
	RACMO	32,254 (78.4%)	8,701 (21.1%)	191 (0.5%)	41,146
	CARRA	160,588 (79.5%)	41,210 (20.4%)	191 (0.1%)	201,989

Table 2. Number and percentage of observational data points fitted for each model and time period by type and total.

The temporal resolution of SUMup data varies between method types: ice cores, mass balance profiles and radar estimates (with the exception of surface layers) provide annual to multi-annual averages; snow pits span between 5-12 months; stake measurements range from daily up to two years; and snowfox sensors record at weekly intervals. Sub-monthly data are resampled to monthly sums to match the temporal resolution of the model outputs. Annual or multi-annual means comprise ∼80% of the resulting data (Table 2).

Measurement start and end dates are rounded to the nearest month start/end to align with the monthly model outputs. In cases where this rounding produces a mismatch of greater than 15% of the total measurement duration, the data is excluded to avoid introducing artificial biases from temporal misalignment. For measurements where only the start year and end year are reported in SUMup, start and end dates are inferred from the original studies if possible. For example, some sources measuring cores with H_2O_2 dating use summer peaks to derive annual accumulation (e.g. Kjær et al., 2021), while others use mid-winter peaks (e.g. Miège et al., 2013). When details of measurement dating are not provided in the source text, default values corresponding to the first and last days of the reported year(s) are assigned. This applies to 48% of entries for 1960–2022, 43% for 1980–2022, and 37% for 1991–2022.

We assign a dating uncertainty to every SUMup record to account for errors in the time bounds of each SMB measurement, stated in months. This uncertainty is taken from the original study, if stated, otherwise, a default value is assigned based on commonly stated dating uncertainties in studies using similar methods. For radar and ice/firn-core measurements, we assign a dating uncertainty of 12 months to account for the possibility of a missed annual layer. Snow pits, for which precise start dates are unknown, are assigned a dating uncertainty of 2 months, while stake measurements and snowfox sensors, which have defined start and end dates are given a dating uncertainty of 0. Estimates from mass balance profiles are also assigned an uncertainty of 0. The dating uncertainty is implemented as a Gaussian weighted uncertainty distribution, allowing the model output to be bias-adjusted against each measurement within the given uncertainty range.

The latitude and longitude coordinates of each measurement are then matched with the nearest grid cell for each model. Radar data points from the same source and year range, which are thus not independent, are grouped and averaged within grid cells, reducing the computational time for the fit. This leads to a different number of individual data points for fitting each model due to their differing spatial resolutions (Table 2). This approach effectively smooths radar data to a greater degree for the lower-resolution models.

3 Methods

3.1 EOF analysis

Our method relies on Empirical Orthogonal Function (EOF) analysis, performed via a Principle Component Analysis (PCA) on model accumulation output within the PROMICE ice mask, using the eofs.xarray module from the $eofs$ Python library (Dawson, 2016).

The model output, $\mathbf{X}(x,y,t)$, is first centred by removing the temporal mean, $\mathbf{M}(x,y)$, and the climatology, $\mathbf{C}(x,y,m)$, where $\mathbf{C}$ is the mean deviation of each month, m, from the temporal mean. The EOFs, $\mathbf{EOF}(x,y)$, reveal the preferred patterns of spatial variability, while the principle components, $\mathbf{PC}(t)$, describe their monthly temporal evolution for each mode, i.

The reconstructed model accumulation, $\mathbf{Acc}(x,y,t)$ can thereby be expressed as:

$$\mathbf{Acc}(x,y,t) = \mathbf{M}(x,y,t) + \mathbf{C}(x,y,m) + \sum_{i=1}^{N} \mathbf{PC}_i(t) \cdot \mathbf{EOF}_i(x,y). \tag{8}$$

The EOF computation is weighted by the square root of the fractional area of each cell to ensure that the covariance-based EOFs reflect area-averaged variability. In this study, we limit the adjustment to the first 10 EOF modes, capturing 86-91$\%$ of the variance in the output, while avoiding over-fitting noise captured by the higher order modes. Using a truncation such as this, a truncation residual term, $\mathbf{R}(x,y,t)$, is introduced to describe the remaining variability and noise not captured by the first 10 modes. Further details of the EOF method are provided in appendix A1.

3.2 The model

The SUMup dataset is used to find a set of coefficients to adjust each component of the accumulation reconstruction, derived by fitting the in-situ SUMup data points using the python package scipy.optimize.least_squares for least-squares optimisation (Virtanen et al., 2020). The bias-adjusted reconstructed accumulation, $\mathbf{Acc}(x,y,t)$ is then expressed as:

$$\mathbf{Acc}(x,y,t) = \ a_0 + \mathbf{M}(x,y,t) + b_0\mathbf{C}(x,y,m) + \sum_{i=1}^{10} (b_i\mathbf{PC}_i(t) + a_i)\,\mathbf{EOF}_i(x,y) + \mathbf{R}(x,y,t), \tag{9}$$

where a_0 adjusts the mean, $\mathbf{M}(x,y)$, a_i adjust the EOFs, $\mathbf{EOF}_i$, b_0 adjusts the climatology, $\mathbf{C}$, b_i adjusts the PCs, $\mathbf{PC}_i$, and the truncation residual term, $\mathbf{R}$ is not adjusted. The initial guess (no adjustment) is set to 0 for the time-independent a parameters and 1 for the time-dependent b parameters. Using 10 EOFs results in 22 free parameters.

The dominant EOF patterns and associated PCs are often interpreted in terms of physical processes that drive climate variability, however, here they are solely used to create a smooth, reduced-dimensional basis for bias estimation.

We minimise the misfit between SUMup observations and modelled accumulation using residuals scaled to an annual basis, giving proportionally greater weight to higher-resolution measurements. Due to the temporal uncertainty inherent in much of the SUMup dataset, of which $\sim$80% consists of annual or multi-annual averages, the precise timing of individual accumulation events is often uncertain in the observations. Therefore, to prevent over-fitting and mitigate the impact of dating errors, we implement Tikhonov regularisation on the b-parameters, constraining them towards the initial guess via a regularisation parameter λ. The optimum λ is found through 5-fold cross-validation, determined by where the average mean squared error (MSE) of the residuals is minimised. To account for potential dependencies within SUMup, we ensure that temporally or spatially linked measurements, such as data points from the same ice core, snow pit, stake network, or radar horizon, are grouped and assigned to the same fold during cross-validation. The assignment of data to folds is otherwise random. The optimal λ is determined independently for each model and evaluation period. For 1991-2022 period, the cross-validation yields λ values of 8.9 for HIRHAM, 15.8 for MAR, 8.9 for RACMO, and 12.6 for CARRA. Over the 1980-2022 period, the corresponding values are 14.1 for HIRHAM, 11.2 for MAR, and 11.2 for RACMO, and for 1960-2022, the optimal λ for HIRHAM and MAR are again 14.1 and 11.2.

To reduce the influence of outliers, several data transformation techniques, including log and arcsinh transforms, were tested and evaluated using the same cross-validation approach. However, as these provided no measurable improvement in fit quality, subsequent development and optimisation was performed in linear space. As an alternative, the five loss functions available in the scipy.optimize.least_squares package were evaluated across a range of outlier threshold values (f_scale). The arctan loss function with f_scale = 1 m yr^{-1} was found to provide the best performance on average in MSE reduction, and was therefore adopted across all models for consistency.

3.3 Bias Analysis

To assess the statistical significance of reconstructed biases, we test the null hypothesis that the observed accumulation bias, defined as the difference between the original and bias-adjusted fields, arises solely from internal inter-annual variability. Annual accumulation anomalies are modelled as a first-order autoregressive (AR(1)) process, with parameters estimated from the original model output. For each model and fitting period, we generate k AR(1) realisations of synthetic bias, whose cumulative sums form a Monte Carlo null distribution. Statistical significance is assessed using a two-sided p-value, defined as the fraction of simulations whose absolute cumulative bias exceeds that of the observed value. Details of the implementation are provided in appendix A2.

For spatial bias maps (Figs. 3, 4, A4), this test is applied independently at each grid cell, accounting for temporal autocorrelation but not spatial covariance. Grid cells with $p < 0.05$ are indicated by hatching. For domain-wide mean biases (Tables 4, A1, A2, Fig. 4 (in-panel mean values)), the test is applied to a single spatially aggregated time series for each domain, such that p-values account for both temporal autocorrelation and implicitly for spatial covariance. Statistically significant mean biases (p<0.05) are highlighted in bold.

For Table 3, where metrics are derived from direct comparison between individual observations and corresponding model grid cell values over differing time scales (monthly to multi-annual), inter-annual variability cannot be defined in a consistent or meaningful way. Statistical significance of mean bias and RMSE changes is therefore assessed using 95% confidence intervals obtained from 1,000 non-parametric bootstrap resamples.

Bias-adjusted mean accumulation values are provided with uncertainty intervals, estimated through spatial cross-validation. The adjustment model is trained by withholding all observations from one of the seven ice-sheet basins and validated on the remaining basin in turn. The uncertainty, σ, is expressed as the standard deviation of the seven reconstructions, R_i, relative to the mean the full-data reconstruction, $\bar{R}$:

$$\sigma = \sqrt{\frac{1}{7}\sum_{i=1}^{7}\left(\bar{R}_i - \bar{R}\right)^2}. \tag{10}$$

This value, representing the sensitivity of the adjusted reconstructed mean accumulation to variations in the training dataset, is hereafter referred to as cross-validation uncertainty.

Model bias is quantified both as the net difference (original mean minus bias-adjusted mean) and as a relative bias, calculated at each grid point as:

$$Bias\ \% = \frac{\overline{X} - \overline{X'}}{\overline{X}} \cdot 100, \tag{11}$$

where $\overline{X}$ is the original model temporal mean and $\overline{X'}$ is the bias-adjusted temporal mean. Seasonal biases, grouped by winter (DJF), spring (MAM), summer (JJA) and autumn (SON), are reported in terms of relative bias.

The bias-adjustment is also evaluated through analysis of linear trends and accumulation sensitivity to temperature, evaluated by grid-point-wise and domain-wide regressions. Sensitivity is defined as the percent change in accumulation per degree Celsius, derived from the Clausius-Clapeyron relationship (Clausius, 1850; Clapeyron, 2006) describing the saturation water vapour pressure, e_s as a function of temperature, T. Using a similar approach to Nicola et al. (2023) and Bochow et al. (2024), the Clausius-Clapeyron relationship can be expressed as:

$$\frac{\mathrm{dln}e_s}{\mathrm{d}T} = \frac{L}{R_v T^2} = k, \tag{12}$$

where L is the latent heat of vaporisation, R_v is the specific gas constant for water vapour and k is the growth constant. Assuming precipitation, P, scales with the saturation vapour pressure, the response of precipitation to temperature is commonly modelled via a log-linear relationship (Nicola et al., 2023; Bochow et al., 2024). We extend this approach to net accumulation, assuming that under cold, high-latitude conditions where sublimation and evaporation are minimal relative to precipitation, accumulation approximately scales with precipitation. Therefore we fit $\ln(Acc)$ against Northern Hemisphere mean temperature anomalies from the Hadley Centre dataset (Morice et al., 2021, HadCRUT5 analysis), which combines near-surface (2 m) air temperature and sea surface temperature (SST) anomalies. The growth factor, k, is determined from the slope of the linear regression, and therefore represents the fractional change in precipitation per degree Celsius. To express this as a percent change, we define the sensitivity, s, expressed by Bochow et al. (2024):

$$s = 100 \times \left(e^k - 1\right), \tag{13}$$

where s is the percent change in accumulation per degree of warming.

A sensitivity analysis comparing HadCRUT5 with Berkeley Earth (Rohde and Hausfather, 2020) and GISTEMP (Lenssen et al., 2024) reconstructions confirms that the choice of dataset has negligible impact on the results over the post 1960 period investigated here.

4 Results

4.1 Bias-Adjustment Coefficients

Bias-adjustment coefficients quantify how each component of the model decomposition (eq. 9) is scaled to fit SUMup data (Fig. 2).

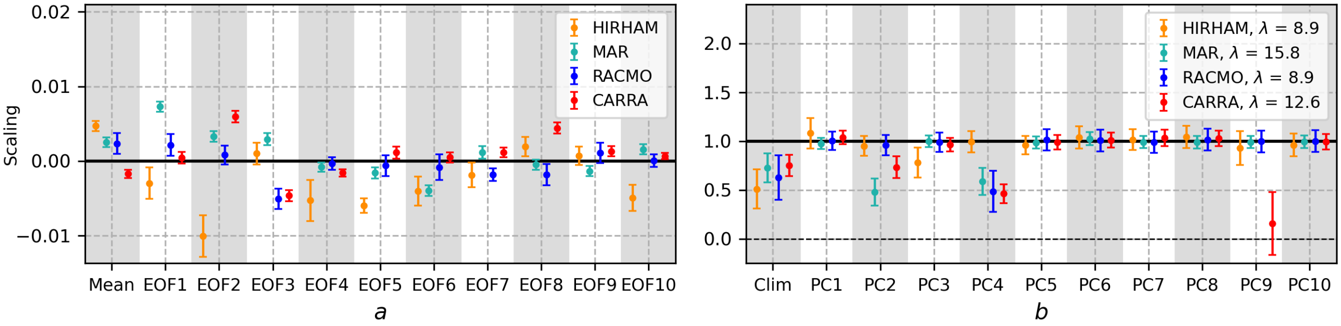

Figure 2. Bias-adjustment coefficients derived from fitting the 1991-2022 overlap period using the arctan loss function. Error bars represent the uncertainty in the parameter estimates, reflecting the confidence in the fitted coefficients rather than spatial variability. The initial guess (no adjustment) is denoted by the solid black line. Left: a parameters adjusting the time-independent mean bias and 10 EOF modes. Right: b parameters adjusting the time-dependent climatology and 10 PC modes, with λ values derived independently for each model via cross-validation.

Adjusting the mean, a_0 is positive for HIRHAM, MAR and RACMO, reflecting a mean negative bias, but negative for CARRA, to correct a mean positive bias. The EOF coefficients ($a_1 - a_{10}$) scale the amplitude of spatial variability patterns (EOF modes shown in appendix Fig. A5). HIRHAM shows the greatest spread in EOF coefficients, with a standard deviation of 0.004, while RACMO shows the smallest (0.002). Differences in the EOF coefficients between models are associated with differing EOF patterns, bias structures, and radar grouping.

The b coefficients are influenced by the regularisation parameter, λ, which penalises deviations from the initial guess to account for the temporal uncertainty in observational dating. Models with higher λ are more strongly constrained to remain close to the initial guess. Adjusting the climatology, b_0 is scaled down for all models to between 0.51 (HIRHAM) and 0.75 (CARRA), reflecting the smoothing of sub-annual variability due to the the dominance of annual/multi-annual measurements constituting $\sim$80% of the SUMup data (table 2). Most PC adjustment coefficients ($b_1 - b_{10}$) remain close to the initial guess of 1, with a few notable exceptions (MAR PC2, PC4 for MAR, RACMO and CARRA, and PC9 CARRA). Despite the largest regularisation terms, MAR (λ=15.8) and CARRA (λ=12.6) show the greatest spread, with standard deviations of 0.18 and 0.29, respectively, driven by strong scaling of a few select coefficients.

4.2 Bias-Adjustment Assessment Metrics

Prior to bias-adjustment, CARRA exhibits the largest statistically significant mean point-wise bias of +10.1% compared to observations (Table 3), followed by HIRHAM with a consistent significant negative mean bias of -7.5% to -7.4% over all fitting periods. MAR exhibits small initial biases, which are statistically significant in the 1960–2022 (-0.5%) and 1991–2022 (+0.7%). RACMO is the only model to show non-significant negligible mean bias ($\sim$0%) in both fitting periods.

Period	Model	Bias	Bias$_{\text{adj}}$	RMSE	RMSE$_{\text{adj}}$	ΔRMSE	R	R$_{\text{adj}}$	ΔR
		[%]	[%]	[mm yr^{-1}]	[mm yr^{-1}]	[%]			[%]
1960–2022	HIRHAM	**−7.4**	+0.2	129	122	-5.4	0.84	0.85	+1.2
	MAR	**−0.5**	-0.1	127	110	**−13.6**	0.88	0.88	+0.7
1980–2022	HIRHAM	**−7.5**	+0.3	132	126	-4.6	0.84	0.85	+1.0
	MAR	-0.1	-0.0	129	111	**−14.1**	0.88	0.89	+0.7
	RACMO	-0.0	+0.1	123	117	-5.2	0.88	0.89	+0.5
1991–2022	HIRHAM	**−7.4**	+0.3	133	131	-1.6	0.85	0.85	+0.2
	MAR	**+0.7**	-0.1	130	112	**−13.7**	0.89	0.89	+0.6
	RACMO	-0.0	0.0	119	115	-3.8	0.89	0.90	+0.3
	CARRA	**+10.1**	-0.1	110	99	**−10.0**	0.89	0.90	+0.8

Table 3. Model mean bias, root mean square error (RMSE), and correlation (R) before and after bias adjustment, based on a point-wise comparison with SUMup data (with radar values averaged within grid cells). Bias is expressed as the mean percentage deviation relative to SUMup, $100 \times \langle \text{model} - \text{SUMup} \rangle / \langle \text{SUMup} \rangle$. Bold values indicate statistically significant mean bias or RMSE improvement.

After adjustment, mean bias is reduced to near-zero in all models, to within ±0.1% for MAR, RACMO and CARRA and +0.2%-+0.3% for HIRHAM. RMSE decreases by 1.6-14.1%, representing significant reductions for MAR and CARRA, while correlation improves modestly by 0.3-1.2%.

4.3 Mean Accumulation and Spatial Bias Patterns

Before bias-adjustment, all models share similar spatial patterns of mean accumulation. The large-scale structure of accumulation remains largely unchanged following adjustment, however, marked differences in spatial bias patterns reveal considerable differences between models (Fig. 3).

HIRHAM, MAR and RACMO are consistently biased low in relative mean bias over all periods (Table 4). In HIRHAM, negative bias dominates most of the ice-sheet, reaching -50% in the north and north-east basins. High-accumulation regions in the south-west and south-east basins contribute disproportionately to net bias, where underestimation locally exceeds 150 mm yr^{-1}. MAR also underestimates across much of the ice-sheet, with biases reaching -40% in the north and north-east basins, but differs from HIRHAM through a pronounced fringe of positive bias in the south and central-east, exceeding 150 mm yr^{-1}. RACMO exhibits the smallest mean bias of all models, with a modest -4% underestimation over the ice-sheet in both the 1980-2022 and 1991-2022 periods. Negative relative bias is most prominent in the north-east basin, reaching -30%,

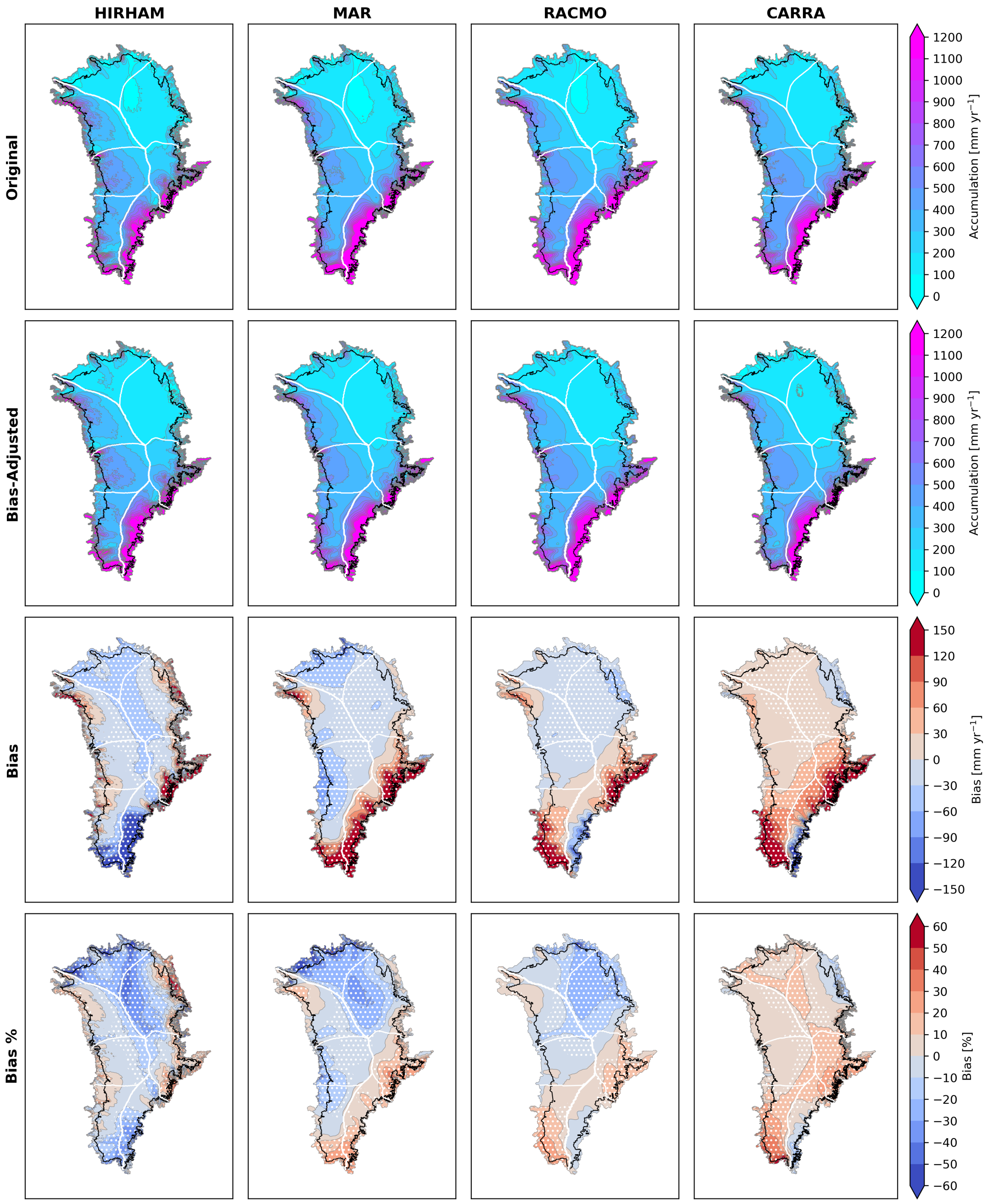

Figure 3. Spatial patterns of of model mean accumulation and bias over 1991-2022. First row: original mean model accumulation. Second row: bias-corrected mean accumulation. Third row: mean net bias (mm yr^{-1}), $\langle \text{original} - \text{adjusted} \rangle$. Fourth row: mean relative bias (eq. 11). Hatched regions indicate statistically significant biases ($p < 0.05$). The black line indicates the accumulation zone boundary, and white lines show PROMICE drainage basins boundaries. Maps for full model periods are provided in the appendix, Fig. A4.

Period	Model	Ice Sheet			Accumulation Zone			Ablation Zone		
		Acc	**Acc$_{\text{adj}}$**	**Bias**	**Acc**	**Acc$_{\text{adj}}$**	**Bias**	**Acc**	**Acc$_{\text{adj}}$**	**Bias**
		[mm yr^{-1}]	[mm yr^{-1}]	[mm yr^{-1}]	[mm yr^{-1}]	[mm yr^{-1}]	[mm yr^{-1}]	[mm yr^{-1}]	[mm yr^{-1}]	[mm yr^{-1}]
1960–2022	HIRHAM	434	458 ± 26	**-25 (-15%)**	364	393 ± 18	**-29 (-15%)**	687	695 ± 59	-8 (-15%)
	MAR	418	393 ± 12	**$+26$ (-13%)**	393	375 ± 9	**$+18$ (-9%)**	512	459 ± 22	**$+53$ (-28%)**
1980–2022	HIRHAM	441	467 ± 27	**-26 (-13%)**	369	400 ± 16	**-30 (-14%)**	700	710 ± 65	-10 (-10%)
	MAR	424	400 ± 11	**$+24$ (-8%)**	397	380 ± 8	**$+17$ (-8%)**	523	475 ± 20	**$+49$ (-8%)**
	RACMO	440	425 ± 13	**$+15$ (-4%)**	388	381 ± 9	$+7$ (-5%)	612	573 ± 25	**$+39$ (0%)**
1991–2022	HIRHAM	446	469 ± 24	**-23 (-11%)**	374	404 ± 14	**-31 (-12%)**	709	704 ± 58	$+5$ (-6%)
	MAR	432	412 ± 12	**$+20$ (-7%)**	404	389 ± 9	**$+15$ (-7%)**	533	494 ± 23	**$+39$ (-8%)**
	RACMO	446	435 ± 10	$+11$ (-4%)	393	389 ± 7	$+4$ (-5%)	619	586 ± 21	**$+33$ (0%)**
	CARRA	451	408 ± 8	**$+43$ ($+9\%$)**	427	387 ± 6	**$+39$ ($+9\%$)**	546	489 ± 17	**$+58$ ($+10\%$)**

Table 4. Mean annual accumulation before (Acc) and after (Acc_{adj}) bias adjustment over the ice sheet, accumulation zone, and ablation zone, with corresponding mean bias. Bias-adjusted values are shown with cross-validation uncertainties (eq. 10). Bias is reported as the net difference ⟨original – adjusted⟩ and relative bias (eq. 11). Statistically significant biases ($p < 0.05$) are highlighted in bold. Equivalent spatially aggregated sums (Gt yr^{-1}) are provided in Appendix Table A1, with temporal evolution of net and cumulative bias shown in Appendix Fig. A6.

while high positive net occurs in the south-west and central-east basins, exceeding 150 mm yr^{-1}. Unlike MAR, RACMO shows a small region of negative bias along the south-east margin, reaching up to -120 mm yr^{-1}.

CARRA exhibits the only mean positive relative bias of the models, at +9% over the ice sheet. The largest net biases are similarly associated with high-accumulation regions in the south and east, with positive bias exceeding +150 mm yr^{-1} in the south-west and central-east basins. Like RACMO, CARRA exhibits a narrow band of negative bias along the south-east margin, with values exceeding -150 mm yr^{-1}.

Relative mean bias decreases in later fitting periods. Over the ice-sheet, HIRHAM bias reduces from -15% (1960-2022) to -13% (1980-2022) to -11% (1991-2022), MAR decreases from 13% to 8% to to 7%, while RACMO remains approximately constant. Similar trends occur in the accumulation and ablation zones.

Within the observation-rich accumulation zone, inter-model standard-deviation in mean accumulation is reduced by 68% following adjustment for 1991-2022. MAR, RACMO, and CARRA converge closely, scaled down to 389±9, 389±7 and 387±6 mm yr^{-1}, respectively. HIRHAM, initially at 374 mm yr^{-1}, is scaled up to 404±14 mm yr^{-1} after adjustment, falling outside the uncertainty bounds of other models.

In the ablation zone, where data coverage is sparse, inter-model standard deviation increases from 68 to 86 mm yr^{-1} for 1991-2022 following adjustment, with larger cross-validation uncertainties reflecting greater spread between individual reconstructions for this region. This disparity in drives an increase in ice-sheet-wide inter-model standard-deviation from 7 mm yr^{-1} to 24 mm yr^{-1} after adjustment.

Apart from RACMO over the 1991–2022 period, all ice-sheet–wide mean biases are statistically significant (Tables 4, A1). All models show significant mean biases in the north, central-east and south-west basins (Table A2), with the south-west representing the greatest net and relative bias for RACMO (+20 to +26 Gt yr^{-1}; +14 to +19%) and CARRA (+34 Gt yr^{-1}; +25%). The south-east basin is also significant for HIRHAM and MAR, constituting their largest net biases, reaching -39 to -54 Gt yr^{-1} (-17 to -25%) for HIRHAM and +30 to +33 Gt yr^{-1} (+14 to +16%) for MAR, while biases are non-significant for RACMO and CARRA (within ±2%). The north-east basin is significant for MAR and RACMO (all periods) and HIRHAM (1960-2022, 1980–2022), while MAR and CARRA also show significant biases in the central-west basin. The north-west basin is not statistically significant for any model and consistently exhibits the smallest net and relative biases.

4.4 Seasonal Bias Patterns

Seasonal pattern biases show strong seasonal contrasts (Fig. 4). All models show a seasonal shift in ice-sheet-wide relative mean biases, from more negative (or less positive) in colder months towards least negative (or most positive) in autumn.

For HIRHAM, MAR and RACMO, the greatest negative relative biases occur in winter and spring, accompanied by the most spatially extensive regions of statistically significant bias. Significant negative biases are concentrated in the north and north-east basins across all three models, extending to the south for HIRHAM and MAR. In summer and autumn, these models exhibit an expanded area of weak positive relative bias (up to $\sim$20%) in the north-west in the summer, which retreats towards central regions in autumn.

In domain-wide means, HIRHAM biases are significant across all domains in spring and summer, coinciding with the seasons of greatest negative net ice-sheet–wide bias, while MAR and RACMO show their largest net biases and statistically significant mean biases across all domains only in autumn.

CARRA maintains positive bias in all seasons, with minimum relative bias in the winter and spring and a maximum in autumn, which coincides with the highest net mean bias and most spatially extensive significant biases. Mean biases are significant in all seasons and domains except summer.

4.5 Temporal Trends

Spatial patterns of temporal trends reveal a pronounced east-west contrast in all models (Fig. 5). Positive trends dominate east of the central ice divide and largely negative trends to the west. This behaviour is largely preserved after bias-adjustment, with a few exceptions. HIRHAM shows slightly expanded regions of positive trends in the north-west basin, while isolated areas of positive trends present prior to adjustment in MAR, RACMO and CARRA become negative in this basin. Consequently, spatial patterns and basin-wise means (Table A3) in MAR, RACMO and CARRA show closer agreement after adjustment, while HIRHAM diverges.

In all models, the strongest trends occur in the south-east, with basin mean values of up to 66 mm yr^{-1} decade^{-1} (Table A3), contrasted with strong negative means in the south-west.

ice-sheet-wide mean accumulation trends are positive across all models, fitting periods, and spatial domains, and bias adjustment generally leads to a small reduction in trend magnitude (typically $\leq$2 mm yr^{-1} decade^{-1}). Notable exceptions include

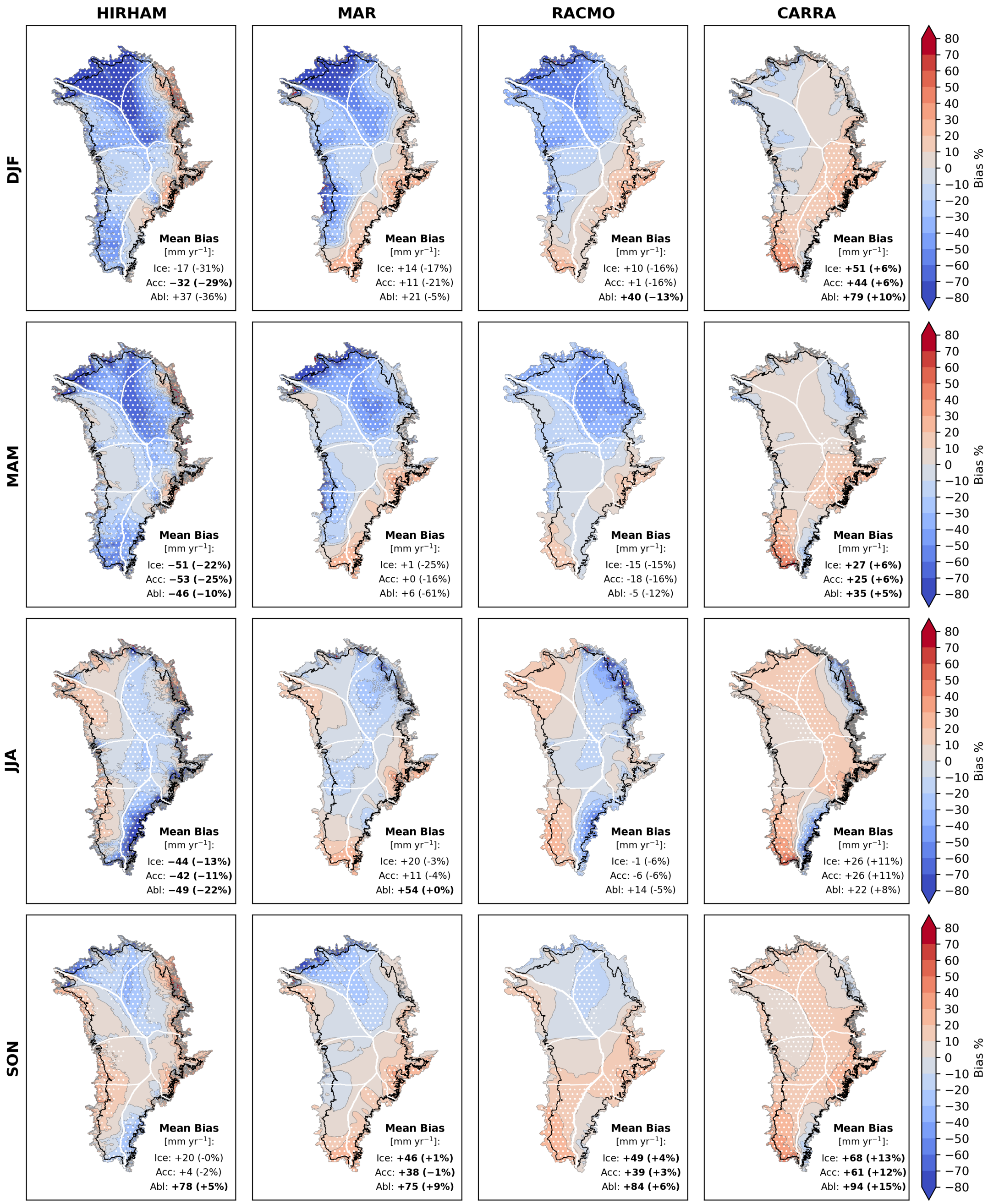

Figure 4. Model mean seasonal relative bias over the 1991-2022 common period, calculated by (eq. 11) for each season. Hatched regions indicate statistically significant biases ($p<0.05$). In-panel labels show seasonal mean bias values over the ice-sheet (Ice), accumulation zone (Acc) and ablation zone (Abl), with statistically significant biases indicated in bold.

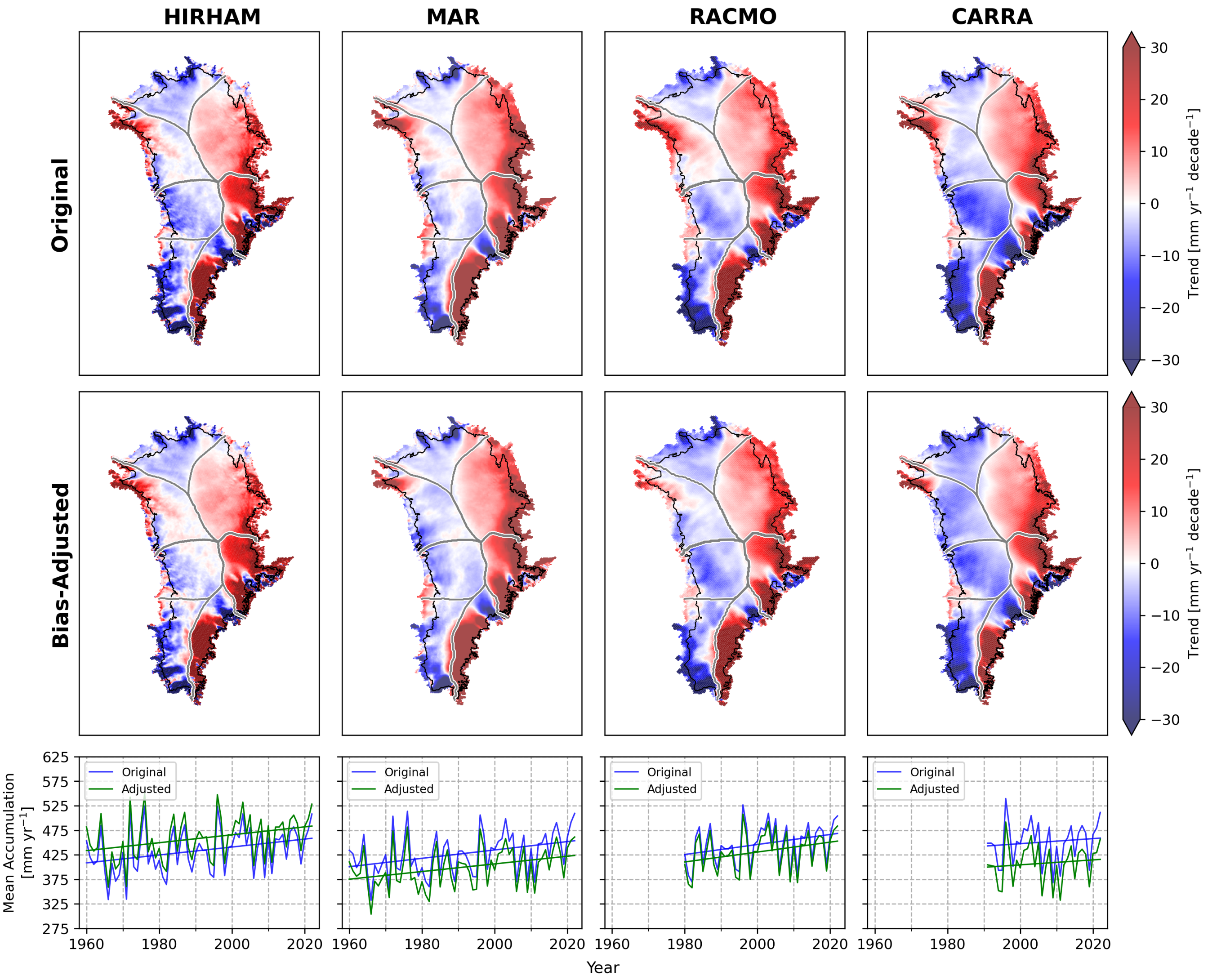

Figure 5. Temporal regressions before and after bias-adjustment. Upper: grid-point-wise regression for the 1991-2022 fitting period, representing spatial variation in linear trends. Lower: mean annual accumulation over the ice sheet with linear fits for HIRHAM (1960-2022), MAR (1960-2022), RACMO (1980-2022) and CARRA (1991-2022).

HIRHAM, for which bias adjustment maintains or slightly increases trend magnitudes, and the CARRA ablation zone trend, where trends increase marginally by 0.3 mm yr^{-1} decade^{-1} following adjustment.

MAR shows the strongest mean trends overall, coupled with the lowest p-values, while CARRA shows the weakest trends and highest p-values. Confidence intervals widen and p-values increase as earlier data are excluded from the fitting period, reflecting the reduced temporal coverage and greater influence of inter-annual variability in shorter records.

		Ice Sheet		**Accumulation Zone**		**Ablation Zone**	
Period	**Model**	**Trend**	**Trend$_{\mathbf{adj}}$**	**Trend**	**Trend$_{\mathbf{adj}}$**	**Trend**	**Trend$_{\mathbf{adj}}$**
		[mm yr^{-1}decade^{-1}]		[mm yr^{-1}decade^{-1}]		[mm yr^{-1}decade^{-1}]	
1960–2022	HIRHAM	8.1 ± 5.9, p=0.01	8.1 ± 5.9, p=0.01	6.4 ± 4.9, p=0.01	6.4 ± 4.9, p=0.01	14.3 ± 10.0, p=0.01	14.3 ± 10.0, p=0.01
	MAR	8.4 ± 5.4, $p<0.01$	7.7 ± 5.2, $p<0.01$	7.0 ± 5.1, p=0.01	6.4 ± 4.9, p=0.01	13.5 ± 6.9, $p<0.01$	12.3 ± 6.7, $p<0.01$
1980–2022	HIRHAM	9.8 ± 9.6, p=0.05	10.0 ± 9.4, p=0.04	7.7 ± 8.2, p=0.07	7.9 ± 8.0, p=0.05	17.2 ± 15.3, p=0.03	17.6 ± 15.0, p=0.02
	MAR	13.6 ± 9.1, $p<0.01$	11.4 ± 8.5, p=0.01	12.4 ± 8.5, p=0.01	10.2 ± 7.8, p=0.01	17.7 ± 12.1, p=0.01	15.5 ± 11.7, p=0.01
	RACMO	10.0 ± 9.5, p=0.04	9.8 ± 9.3, p=0.04	8.9 ± 8.8, p=0.05	8.8 ± 8.6, p=0.05	13.4 ± 12.3, p=0.03	13.4 ± 12.1, p=0.03
1991–2022	HIRHAM	8.7 ± 15.2, p=0.26	10.8 ± 13.5, p=0.12	6.7 ± 12.9, p=0.31	8.4 ± 11.4, p=0.15	15.9 ± 24.1, p=0.20	19.5 ± 22.2, p=0.09
	MAR	13.0 ± 14.5, p=0.08	12.0 ± 13.3, p=0.08	11.7 ± 13.8, p=0.10	10.6 ± 12.3, p=0.10	17.9 ± 18.8, p=0.07	17.2 ± 18.2, p=0.07
	RACMO	8.6 ± 15.1, p=0.26	7.9 ± 14.6, p=0.29	7.4 ± 14.1, p=0.30	6.7 ± 13.5, p=0.33	12.5 ± 19.3, p=0.21	11.9 ± 18.9, p=0.22
	CARRA	5.1 ± 15.9, p=0.52	5.0 ± 15.3, p=0.52	3.9 ± 15.0, p=0.60	3.7 ± 14.4, p=0.61	9.8 ± 20.5, p=0.35	10.1 ± 19.5, p=0.31

Table 5. Spatial mean linear trends in accumulation over the ice sheet, accumulation zone, and ablation zone before and after bias adjustment. Trends are reported with confidence intervals and p-values. Basin-wise mean trends are provided in appendix Table A3.

4.6 Temperature Sensitivity Analysis

Spatial patterns of temperature sensitivity share a similar spatial structure to the temporal regressions (6). MAR shows the strongest positive sensitivities, concentrated in the north- and south-east exceeding +25 % K^{-1} locally, while CARRA shows the most widespread negative sensitivities, reflected by the weakest mean responses (Table 6). Bias-adjustment reduces positive sensitivities in the north-west for MAR, RACMO and CARRA, resulting in near zero values for 1991-2022 (Table A4), while HIRHAM's positive trends in this region remain relatively consistent.

		Mean Spatial Sensitivity		**Temporal Sensitivity**	
Period	**Model**	**Sensitivity**	**Sensitivity$_{\mathbf{adj}}$**	**Sensitivity**	**Sensitivity$_{\mathbf{adj}}$**
		[% K^{-1}]		[% K^{-1}]	
1960–2022	HIRHAM	8.2	7.2	6.7	6.3
	MAR	8.5	7.3	7.6	7.4
1980–2022	HIRHAM	4.8	4.5	6.1	5.9
	MAR	8.9	7.7	10.0	8.8
	RACMO	6.1	5.6	6.4	6.6
1991–2022	HIRHAM	1.2	2.1	4.6	5.4
	MAR	6.5	6.3	8.4	7.5
	RACMO	3.0	1.9	4.3	4.0
	CARRA	1.1	1.2	2.2	2.9

Table 6. Mean spatial (grid-point wise) and temporal (ice-sheet-wide) accumulation sensitivities derived from linear regressions of log-transformed model accumulation against HadCRUT5 NHT anomalies before and after bias adjustment. Basin-wise spatial mean sensitivities are provided in appendix Table A4.

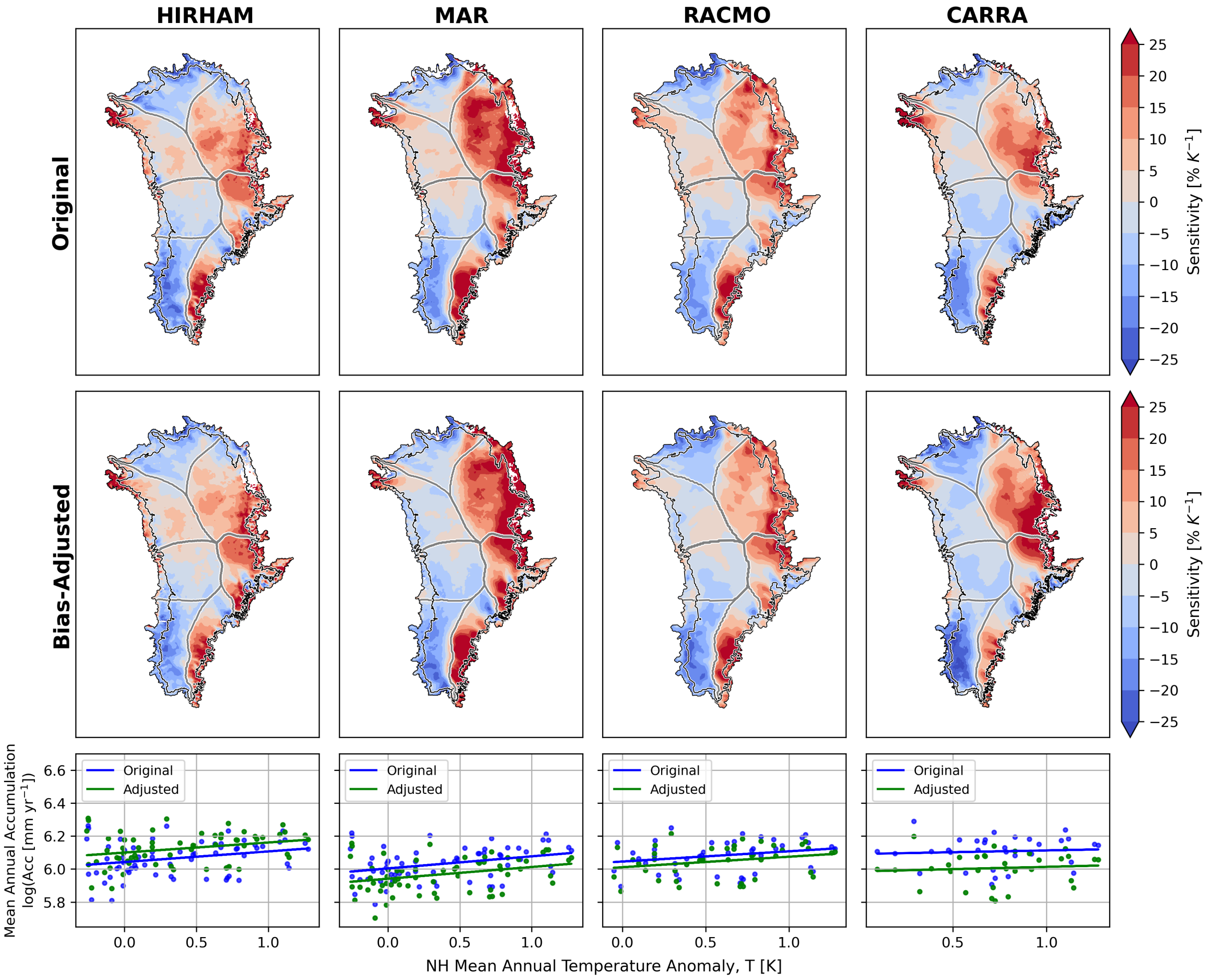

Figure 6. Temperature sensitivity analysis following eq. 12. Upper panels show spatial patterns of sensitivity over 1991-2022, derived from grid-point wise linear regressions of log-transformed annual model accumulation against NHT anomalies from HadCRUT5. Empty grid points resulting from negative accumulation values are excluded from calculation of mean ice-sheet sensitivities. Lower panels show ice-sheet-wide mean annual accumulation (log-transformed) as a function of NHT anomalies with linear fits for HIRHAM (1960-2022), MAR (1960-2022), RACMO (1980-2022) and CARRA (1991-2022).

Mean spatial sensitivities, calculated as the grid-point average of localised responses, differ systematically from the temporal regression-derived sensitivities which reflect the ice-sheet's integrated response to inter-annual temperature variability (Table 6). With the exception of the 1960-2022 period, temporal sensitivities exceed spatial averages. For 1991-2022, CARRA shows the lowest mean sensitivities, with an ice-sheet-wide temporal mean approximately four times lower than MAR, and six times lower in the spatial mean.

Bias adjustment generally reduces both spatial and temporal sensitivity means (Table 6), with the exception of HIRHAM and CARRA for the 1991-2022 period and RACMO for 1980-2022, for which sensitivities increase slightly following adjustment.

5 Discussion

5.1 Mean Bias and Spatial Patterns

Our results indicate that all models exhibit statistically significant ice-sheet-wide mean biases of 4–15% (Table 4), corresponding to 20–77 Gt yr^{-1} (Table A1). Although modest on an annual basis, such biases accumulate substantially over time (Fig. A6). Over a century long simulation, a persistent 10% bias would amount to ∼8,000 Gt, sufficient to alter sea-level rise projections by approximately 25 mm by 2100 (The IMBIE Team, 2020). Using the empirical relationship between SMB and temperature from AR5 (Intergovernmental Panel On Climate Change, 2014, Chapter 13 Supplementary Material), an ∼80 Gt yr^{-1} SMB deviation corresponds to an equivalent warming bias of ∼1°C. This represents a substantial error relative to critical thresholds for Greenland ice-sheet stability, such as the ∼1.6°C threshold identified by Robinson et al. (2012), beyond which the GrIS is expected to undergo irreversible long-term mass loss. If uncorrected, such biases could obscure or misrepresent the proximity to tipping points in climate projections.

Despite low mean biases in MAR and RACMO (Tables 3, 4, A1), consistent with Fettweis et al. (2020), who find MAR3.9.6 and RACMO2.3 outperform 13 other models compared against against GrIS-wide observations, our spatial analysis shows that these low means mask compensating strong positive and negative regional biases (Fig. 3, Table A2), including areas which may exert disproportionate influence on sea-level rise. Mouginot et al. (2019) identify the north-west, south-east, and central-west as the primary contributors since 1972, with 34% of total mass loss attributed to SMB changes. We find that MAR exhibits statistically significant accumulation biases in two of these regions: +9% (+9–12 Gt yr^{-1}) in the south-east and -8 to -9% (-6 to -7 Gt yr^{-1}) in the central-west.

HIRHAM and CARRA exhibit more spatially consistent low and high biases, respectively, with greater statistically significant point-wise (Table 3) and ice-sheet-wide (Table 4). HIRHAM, however, represents the only model with non-significant ablation zone bias, aligning with Fettweis et al. (2020) who find that HIRHAM outperforms other models against observations in the ablation zone.

In contrast, while we find CARRA, biased high by +9 to +10% in point-wise and ice-sheet-wide means (Tables 3, 4), performs worse than both MAR and RACMO, recent studies have found that CARRA shows better agreement with observations relative to other models. Evaluating CARRA and RACMO2.3p2 against daily snow depth data from 9 coastal weather stations in Greenland, van der Schot et al. (2024) report correlation coefficients between CARRA and observations are generally higher than for RACMO, with no clear overestimation or underestimation from either model. Similarly, (Box et al., 2023) evaluate CARRA, ERA5, NHM-SMAP, RACMO2.3p2 and MARv3.11.5 against precipitation data from seven automated weather stations in two regions, four of which are on the ice-sheet, finding that CARRA simulations have the lowest average bias.

The CARRA Data User Guide (Copernicus Climate Change Service, 2021) highlights that the model shows improved agreement with the observations of high-precipitation events than ERA5, whose coarser resolution limits its ability to predict the highest precipitation amounts. However, they note that the model tends to overestimate precipitation compared to in-situ observations over northern Scandinavia. Higher spatial resolution models can better resolve complex topography and associated mesoscale circulation, leading to stronger orographic enhancement of precipitation (Lucas-Picher et al., 2012). While this can improve the representation of intense precipitation events, it may also result in higher mean precipitation relative to coarser-resolution products. Similar resolution-dependent increases in precipitation have been documented for regional climate models over Greenland, where downscaling from $\sim$5 km to $\sim$1 km leads to enhanced precipitation, particularly through increased rainfall contributions (Huai et al., 2022). Consequently, CARRA's tendency towards overestimation may be linked to its higher spatial resolution and sensitivity to orographically driven precipitation extremes.

Common to all models is a strong bias in the south; a region characterised by high snowfall and mountainous topography. Previous studies have identified the south-east, in particular, as a significant source of uncertainty, due to high spatial variability, complex orographic effects and limited observational coverage (Fettweis et al., 2020; Ryan et al., 2020; Koenig et al., 2016; Miège et al., 2013; Burgess et al., 2010).

Notably, HIRHAM significantly underestimates in the south-east basin by up to -25% (Table A2). Lucas-Picher et al. (2012) compare HIRHAM accumulation with ice cores from Andersen et al. 2006; Banta and McConnell (2007) and Bales et al. (2009), finding southern biases generally <10%. Our analysis, using a substantially larger observational dataset including radar-derived accumulation and covering previously unsampled areas, indicates that earlier evaluations may have underestimated biases near the complex southeastern margin.

The northern interior of the ice-sheet contributes disproportionately to relative bias in HIRHAM, MAR and RACMO, with significant local biases of up to 30-50% (Fig. 3). This may reveal a shared tendency between these models to underestimate accumulation at cold, dry, high elevation sites, where atmospheric moisture is limited and snowfall events are infrequent, but significant for accumulation. Langen et al. (2017) also report that at high-elevation sites, HIRHAM5-based simulations underestimate net accumulation by 8–16%.

While the north interior benefits from relatively consistent observational coverage through time, the south-east has sparse coverage prior to 2000 (Fig. A1), and the south-west remains limited throughout. As a result, adjustments in the south are less well constrained, particularly in earlier periods, contributing to greater uncertainty in both regions. This may contribute to the decrease in mean relative bias in later fitting periods (Table 4).

Observations also become increasingly uncertain further back in time: deeper ice-core layers are more prone to miscounting (Steig et al., 2005), and radar horizons are more likely to be misidentified (Bingham et al., 2025), which may lead the bias-correction to apply larger, possibly unnecessary, corrections. Furthermore, the number of observations assimilated into ERA5, which provides boundary conditions for all models, declines drastically in earlier decades (Hersbach et al., 2019), degrading model performance in the past.

5.2 Seasonal Bias and Spatial Patterns

The observed seasonal shift in ice-sheet-wide biases may reflect seasonally varying climatic processes that influence model performance differently over the year–while CARRA exhibits statistically significant biases across all domains in all seasons except summer, HIRHAM shows significant domain-wide biases primarily in spring and summer, and MAR and RACMO only in autumn.

However, seasonal biases must be interpreted within the context of the temporal limitations of the observations, of which only 0.1-0.5% are monthly measurements and ∼80% are annual or multi-annual means (Table 2), with start and end dates often estimated from mid-winter or mid-summer measurement peaks or melt horizons. These dating assumptions, which vary between sources, combined with the filtering of negative SMB measurements, particularly affect the robustness of spring and summer bias estimates. These factors leave a small fraction with which to reliably constrain bias patterns on a seasonal scale (Fig. A2), making them inherently less robust than the long-term annual means.

5.3 Temporal Trends and Temperature Sensitivity

The tendency for the bias-correction to temper mean accumulation trends for MAR, RACMO and CARRA may indicate that these models are overly sensitive to warming air temperatures, while HIRHAM, whose trends are slightly amplified by the adjustment, may be under-sensitive. All models show strong trends in the high accumulation south, coinciding with where net biases are largest. This region is also poorly sampled in earlier periods (Fig. A1). For MAR, RACMO and CARRA, with high positive biases dominating in the south, bias-adjustment reduces accumulation means on average, more strongly in earlier periods fitting periods. Their mean trends are also reduced after adjustment. Conversely, for HIRHAM, initially biased low in the south, mean accumulation is scaled up by the adjustment, more so in earlier periods, and its mean trend is increased. This behaviour may be the result of both stronger corrections applied to earlier, less well-constrained periods.

HIRHAM and MAR's longer historical coverage (1960–2022) provides more statistically robust estimates, supported by lower uncertainties and statistically significant p-values of <=0.01. These longer-term trends are more resilient to inter-annual variability, which can dominate shorter records and obscure underlying trends. As such, the longer records provided by HIRHAM and MAR spanning 1960–2022, likely provide the most statistically reliable estimate of long-term accumulation trends, due to their extended temporal coverage.

Although spatial trend patterns are illustrated for the shorter 1991–2022 period, the strong consistency in the sign and structure across models suggests that the broad-scale spatial contrasts, particularly the east–west contrast and strong southern gradients, are robust features (Fig. 5).

Similarly, spatial patterns of temperature sensitivity (Fig. 6) are largely consistent between models. The patterns identified here share several consistent features with regional sensitivities reported in Buchardt et al. (2012), who find a pronounced east-west contrast in the south. In the south-east, where Buchardt et al. (2012) report sensitivities of +8.2±0.8% K^{-1}, we find basin-mean values ranging from +5.4 to +15.8% K^{-1} (Table A4). In the south-west, their reported sensitivity of -4.0±0.1% K^{-1}, corresponds to predominantly negative basin-mean sensitivities of -13.2 to +2.3 % K^{-1}. Similarly, in the central-east, where they find high sensitivities of +9.2±1.0% K^{-1}, adjusted values range from +8.1 to +20.6% K^{-1}.

In the central-west, however, where Buchardt et al. (2012) report their highest sensitivity of +9.4±0.1% K^{-1}, we find moderate values, which are further reduced or become negative following adjustment, ranging from -4.2 to +2.5 % K^{-1}. Conversely, we find our highest sensitivities in the north-east basin ranging from +7.2 to +22.3 % K^{-1} after adjustment, while

Buchardt et al. (2012) report their lowest sensitivities of +1.5±2.8% K^{-1}. These discrepancies may reflect a temporal shift in accumulation sensitivity in these regions, as Buchardt et al. (2012) derive their estimates from ice cores mostly drilled in the 1970s and 1980s. Meanwhile, the strong east–west contrast in the south and high sensitivities in the central-east basin are consistent between both studies, suggesting these patterns have persisted over time.

5.4 Limitations

The results presented in this study are subject to a number of methodological and observational limitations, which influence the magnitude, spatial structure and inter-model agreement in the final bias-adjusted accumulation, trend and sensitivity estimates.

Firstly, the EOFs are statistical constructs, which represent differing patterns of variability between models (Fig. A5) and fitting period. In this study, we retain 10 EOFs, while higher-order EOFs account for an additional 8–14% of the variance. The higher order modes may represent physically meaningful variability rather than noise, and distinguishing between noise and signal in these higher modes is non-trivial. By construction, the EOF approach introduces a degree of spatial smoothing, meaning that highly localised differences accumulation captured in the observations may not be fully represented in the adjusted fields. Differences in EOF patterns and in how each mode is scaled by the observations may contribute to inter-model differences in the bias-adjusted results. A sensitivity test using up to 15 EOFs shows slight changes in spatial bias patterns and mean accumulation values. Using 15 EOFs reduces the inter-model standard deviation in bias-adjusted mean accumulation over the ice sheet from 23 mm yr^{-1} (10 EOFs) to 20 mm yr^{-1}, although both remain higher than the pre-adjustment standard deviation of 5 mm yr^{-1}. While this change is small relative to the overall level of inter-model agreement, it demonstrates that methodological choices in EOF truncation influence the adjustment outcome.

In addition, the robust loss function, which down-weights extreme deviations while preserving overall model–data agreement, may contribute to instances where the bias-adjustment leads apparent over-correction, further contributing to increased inter-model spread. For example, HIRHAM shifts from a negative point-wise mean bias of -7.4% to a slightly positive bias of $+0.3\%$ (Table 3) and is scaled upward beyond the uncertainty ranges of the other models in the ice-sheet-wide means (Table 4), which otherwise converge within ± 2 mm yr^{-1}. Consequently, cross-validation uncertainties may be underestimated; a complementary measure could use the spread across the four bias-adjusted means, reflecting inter-model differences in addition to training sample uncertainty.

Despite uncertainties associated with the method, comparison of the spatial bias patterns (Fig. 3, row 3) with point-wise biases (Fig. A3) lends confidence that the method captures the dominant bias structures present in the observations. While final mean accumulation values are sensitive to methodological choices, the bias-adjusted maps provide a robust representation of where models are biased according to observations.

Ultimately, however, our results are intrinsically dependent on the quality, representativeness and temporal coverage of the observational data used for bias adjustment. Though the $\sim$2 million data points in SUMup provide substantial statistical power compared to smaller-scale studies, observational uncertainties limit the accuracy of these final products. Through detailed inspection of the SUMup database, we identified and removed a number of erroneous measurements, thereby improving the quality of the input dataset. However, despite extensive filtering and quality control, some erroneous or unrepresentative observations may remain. Radar-derived accumulation measurements, dominate the observational constraints, accounting for approximately 92–99% of the data used in the fitting. These measurements, as well as ice cores, rely on density assumptions, which vary between datasets and introduce further uncertainties. As a result, any systematic bias or methodological limitation inherent to radar surveys will have a pronounced influence on the adjusted fields. Experiments in which radar data were excluded lead to substantially larger apparent model biases and RMSE values. This likely reflects the drastic reduction in sample size and spatial coverage when radar data are omitted, increasing sensitivity to outliers. Continued efforts to improve the calibration of historical radar surveys and to identify outliers in point measurements will therefore be beneficial for any statistical analysis relying on SUMup.

Observational sparsity may also contribute to instances where the bias adjustment does not improve inter-model agreement, particularly in the ablation zone, where high initial inter-model spread further increases after adjustment (Table 4)). Previous studies have similarly found poorer agreement in the ablation area, both between models and observations (Vernon et al., 2013) and between models themselves Fettweis et al. (2020). Characterised by complex topography and strong spatial gradients, the ablation zone remains the most poorly observed, especially in earlier decades with as few as three stake measurements prior to 1970 (Fig. A1).

To improve the accuracy of bias corrections, especially at sub-annual timescales, there is a pressing need for additional high-resolution, ground-truth data such as direct snow-water-equivalent observations that are independent of density assumptions, particularly in the ablation zone and southern ice-sheet where uncertainties are largest. High-temporal-resolution measurements from emerging technologies, such as those based on cosmic ray sensing (e.g. Howat et al., 2018), offer a promising means of providing continuous, density-independent accumulation data. Further work aimed at improving observational coverage and quality would enhance the robustness and reliability of future accumulation estimates.

6 Conclusions and Outlook

We have devised a novel statistical-semi-empirical framework to quantify and correct spatial and temporal biases in gridded model accumulation using any in-situ observational data. By providing spatially complete, bias-corrected accumulation fields, the method offers improved inputs for ice-sheet mass balance studies and other modelling efforts, such as the Ice Sheet Model Intercomparison Project (ISMIP).

Our method is applied here using observational SMB data from the SUMup dataset, to bias-adjust monthly accumulation output from four high-resolution models over the Greenland Ice Sheet: HIRHAM5 (5.5 km, 1960-2022), MAR 3.14 (5 km, 1960-2022), RACMO2.4p1 (11 km, 1980-2022), and CARRA reanalysis (2.5 km, 1991-2022). Relative to SUMup observations, we find point-wise initial mean biases of -7.4% (HIRHAM), -0.5% (MAR), 0.0% (RACMO) and +10.1% (CARRA), which are statistically significant for all models except RACMO. Following bias-correction, all models converge to near-zero mean bias (±0.3%), with RMSE reduced by 2-14% and modest improvements in correlation with observations of $\sim$1%. The resulting bias-corrected mean annual accumulation over the ice sheet are estimated at 469 ±24 mm yr^{-1} (HIRHAM), 412±12 mm yr^{-1} (MAR), 435±10 mm yr^{-1} (RACMO) and 408±8 mm yr^{-1} (CARRA) for the 1991-2022 common period. Inter-model agreement improves substantially in the accumulation zone, with standard deviation in mean accumulation estimates reducing by 68% for 1991-2022, indicating strong convergence where observational coverage is dense.

We compare the original and bias-adjusted accumulation maps to understand spatial bias patterns, identifying significant discrepancies between models. HIRHAM tends to underestimate across the ice-sheet, while CARRA largely overestimates. RACMO exhibits the lowest and only non-significant ice-sheet-wide mean bias for 1991-2022, but exhibits strong spatial contrasts, with a high positive bias in the south and negative bias further north. All models show substantial and statistically significant biases in either the south-east (HIRHAM, MAR), or south-west (RACMO, CARRA), consistent with previous studies, which have attributed substantial biases in the south to issues in resolving orographic precipitation over complex terrain (Langen et al., 2015; Box et al., 2013; Burgess et al., 2010).

Our results demonstrate that modest accumulation biases, if uncorrected, can translate into temperature-equivalent errors large enough to obscure proximity to Greenland ice-sheet tipping points, highlighting the importance of bias-corrected accumulation reconstructions for both process understanding and long-term sea-level projections.

Accumulation biases can also indirectly affect the ice dynamical response of ice-sheet models. Errors in accumulation are absorbed into model calibration of ice dynamical parameters and thereby affect projections. As ice flow is driven by spatial gradients in surface mass balance, accurate spatial distribution pattern of accumulation are essential for simulating realistic ice flow, geometry, and evolution. Reliable projections are thus critically dependent not only on the total SMB, but on capturing its spatial variability across the ice sheet.

These results underline the continued importance of bias-correcting model accumulation using in-situ observations to improve both the spatial fidelity and physical realism of SMB fields. However, the effectiveness of such corrections ultimately depends on the quality and resolution of the available observational data. The dominance of annual and multi-annual means and the scarcity of monthly-resolution data–ultimately limit the accuracy of the bias-adjusted accumulation at sub-annual timescales. To improve the accuracy of bias corrections, future efforts should prioritise expanding high-resolution in situ measurements, including direct snow-water-equivalent observations that are independent of density assumptions.

As our model is configured, new datasets can be readily integrated to further improve bias-correction. Here we have confined the bias-adjustment to accumulation rather than full SMB, due to the lack of sufficient data to constrain runoff. Bias-adjusted accumulation fields may be combined with respective model runoff output to obtain partially bias-adjusted SMB estimates. Our framework can also be adapted to provide bias-corrected fields for other climate variables, as well as other regions such as the Antarctic ice-sheet.

Future work could explore temporal extrapolation of accumulation fields beyond the reanalysis period through leveraging relationships between EOF modes and large-scale climatic drivers. Preliminary analysis indicates that the PCs studied here correlate with climate indices such as the North Atlantic Oscillation, Greenland Blocking Index, and sea ice cover, consistent with previous studies. Modelling PC variability through these indices, combined with proxies such as air temperature, air pressure, ice cores, lake sediments and tree rings, could enable spatially-complete reconstructions of past accumulation patterns.

Code and data availability. Bias-adjusted accumulation fields are available at https://doi.org/10.5281/zenodo.18199332, along with minimal working code to reproduce results for HIRHAM, MAR, RACMO, and CARRA from their EOF decompositions using our processed SUMup dataset. The code can also be applied to other models to derive bias-adjusted fields from gridded accumulation output.

Appendix A: Appendix

A1 Details of EOF Analysis

This appendix provides supplementary details supporting the EOF analysis outlined in Section 3.1.

The model output, $\mathbf{X}(x,y,t)$, is first centred by removing the temporal mean, $\mathbf{M}(x,y)$, and the climatology, $\mathbf{C}(x,y,m)$. The centred data, $\mathbf{X}'(x,y,t)$, is rearranged into matrix form $\mathbf{X}'$, where each row (i) corresponds to a time index, and each column, (j), represents a grid cell, (x_j, y_j). The EOF computation is weighted by the square root of the fractional area of each cell.

To compute the EOFs, the covariance matrix, $\mathbf{\Psi}$, of the anomalies, $\mathbf{X}'$, is calculated as:

$$\mathbf{\Psi} = \frac{1}{N_t - 1}\mathbf{X}'^{\mathrm{T}}\mathbf{X}'. \tag{A1}$$

The EOFs are derived by solving the eigenvalue problem, $\mathbf{\Psi E} = \mathbf{E\Lambda}$, where the eigenvectors, $\mathbf{E}$, are the EOFs and $\mathbf{\Lambda}$ are the eigenvalues arranged in a diagonal matrix. The EOFs are ordered by their corresponding eigenvalues such that the first EOF captures the greatest amount of variance in the data. The Principle Components (PCs) are obtained by projecting the centred data onto the EOFs:

$$\mathbf{PC} = \mathbf{E}^T\mathbf{X}', \tag{A2}$$

where each column of $\mathbf{PC}$ represents the time series of the corresponding mode, expressing how much each mode contributes to the variability through time.

The reconstructed accumulation, $\mathbf{RCM}(x,y,t)$ can thereby be expressed as:

$$\mathbf{RCM}(x,y,t) = \mathbf{M}(x,y,t) + \mathbf{C}(x,y,m) + \sum_{i=1}^{N}\mathbf{PC}_i(t)\cdot\mathbf{EOF}_i(x,y). \tag{A3}$$

It is common to de-trend data prior to EOF decomposition to prevent a long-term linear or low-frequency signal from dominating the leading modes. However, as accumulation trends vary strongly by region and no clear trend was seen to dominate the PCs, there was no advantage in removing a single linear trend. By not de-trending the data, the resulting modes can reflect both the variability and long-term evolution, allowing the bias-adjustment to account for trends in a way that appropriately scales with the rest of the data.

As the common mask introduces some mismatch in glaciarised pixels, SMB components are unavailable in some marginal grid cells. Thus, we calculate extrapolated EOFs, $\mathbf{EOF}_{\mathrm{ext}}$, to fill in these pixels. Within common ice-sheet mask, the anomalies, $\mathbf{X}'_{full}(x,y,t)$ can be expressed as:

$$\mathbf{X}'_{full}(x,y,t) = \sum_{i=1}^{N_t}\mathbf{PC}_i(t)\cdot\mathbf{EOF}_{ext,i}(x,y). \tag{A4}$$

Eq. A4 is projected onto $\mathbf{PC}_i(t)$ and rearranged to obtain an expression for $\mathbf{EOF}_{ext,i}(x,y)$:

$$\mathbf{EOF}_{\mathrm{ext},i}(x,y) = \frac{\mathbf{PC}_i(t)\cdot\mathbf{X}'_{ext}(x,y,t)}{\sum\limits_{i=1}^{N_t}\mathbf{PC}_i^2}. \tag{A5}$$

A2 Significance Testing

The statistical significance of accumulation biases is assessed using a Monte Carlo test, under the null hypothesis that observed biases arise solely from internal inter-annual variability. The bias, $B(t)$, is defined as $B(t) = X(t) - X_{adj}(t)$, where $X(t)$ and $X_{adj}(t)$ are the annualised original and bias-adjusted model accumulation, respectively.

Interannual accumulation anomalies, $X'(t) = X(t) - \overline{X}$, are assumed to follow an AR(1) process,

$$X'_t = \varphi X'_{t-1} + \varepsilon_t, \qquad \varepsilon_t \sim \mathcal{N}\big(0, \sigma^2\big), \tag{A6}$$

with lag-1 autocorrelation, φ, and innovation variance, σ^2, estimated as

$$\varphi = \frac{\sum_{t=1}^{T-1} X'_t X'_{t+1}}{\sum_{t=1}^{T-1} (X'_t)^2}, \qquad \sigma^2 = \frac{1}{T-2} \sum_{t=1}^{T-1} \big(X'_{t+1} - \varphi X'_t\big)^2, \tag{A7}$$

where T is the length of the fitting period in years.

For each model and fitting period, N realisations of synthetic bias, $b(t)$, representing inter-annual variability under the null hypothesis, are generated following eq. A6, with φ and σ^2 estimated from $X'(t)$. Their cumulative sums, $B_{\text{sim}}^{(k)} = \sum_{t=1}^{T} b_t^{(k)}$, define the null distribution, which is compared with the cumulative observed bias, $B_{\text{obs}} = \sum_{t=1}^{T} B(t)$, such that the two-sided p-value is defined as

$$p = \frac{1}{N} \sum_{k=1}^{N} \mathbf{1}\Big(\Big|B_{\text{sim}}^{(k)}\Big| \geq |B_{\text{obs}}|\Big). \tag{A8}$$

For spatial bias maps, this procedure is applied independently at each grid cell with $N = 10{,}000$. Domain-wide mean biases are assessed via a single time series obtained from an area weighted spatial mean (mm yr^{-1}) or sum (Gt yr^{-1}) over each domain, testing with $N = 100{,}000$. Seasonal biases are assessed by averaging monthly accumulation over each season, with AR(1) parameters estimates from the corresponding seasonal anomaly time series.

A3 Appendix Figures

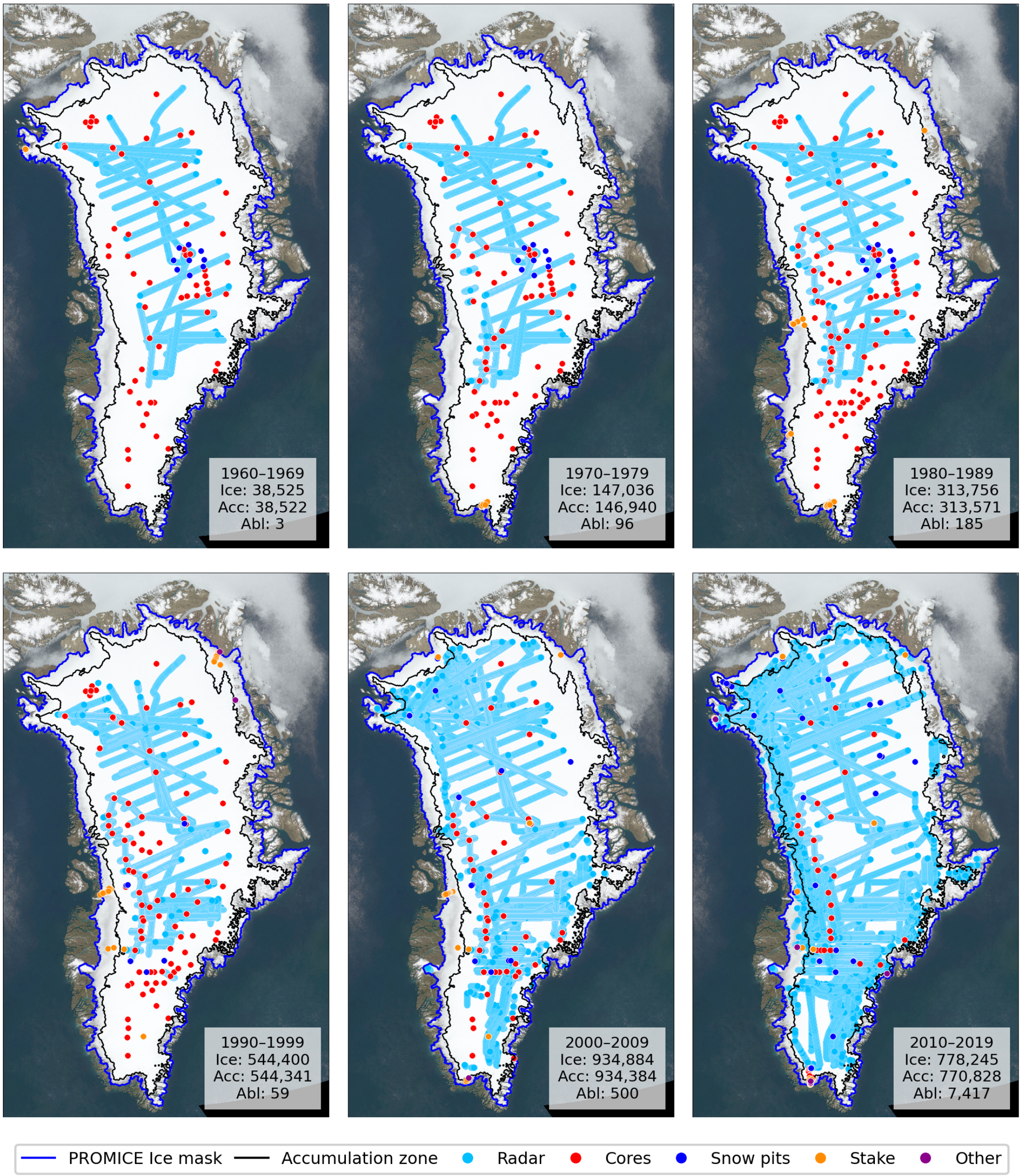

Figure A1. SUMup data distribution by decade, illustrated by measurement type. The method type 'other' includes measurements from mass balance profile and SnowFox sensors. Values for 'Ice', 'Acc' and 'Abl' indicate the total number of data points for the ice-sheet, accumulation and ablation zones before radar grouping.

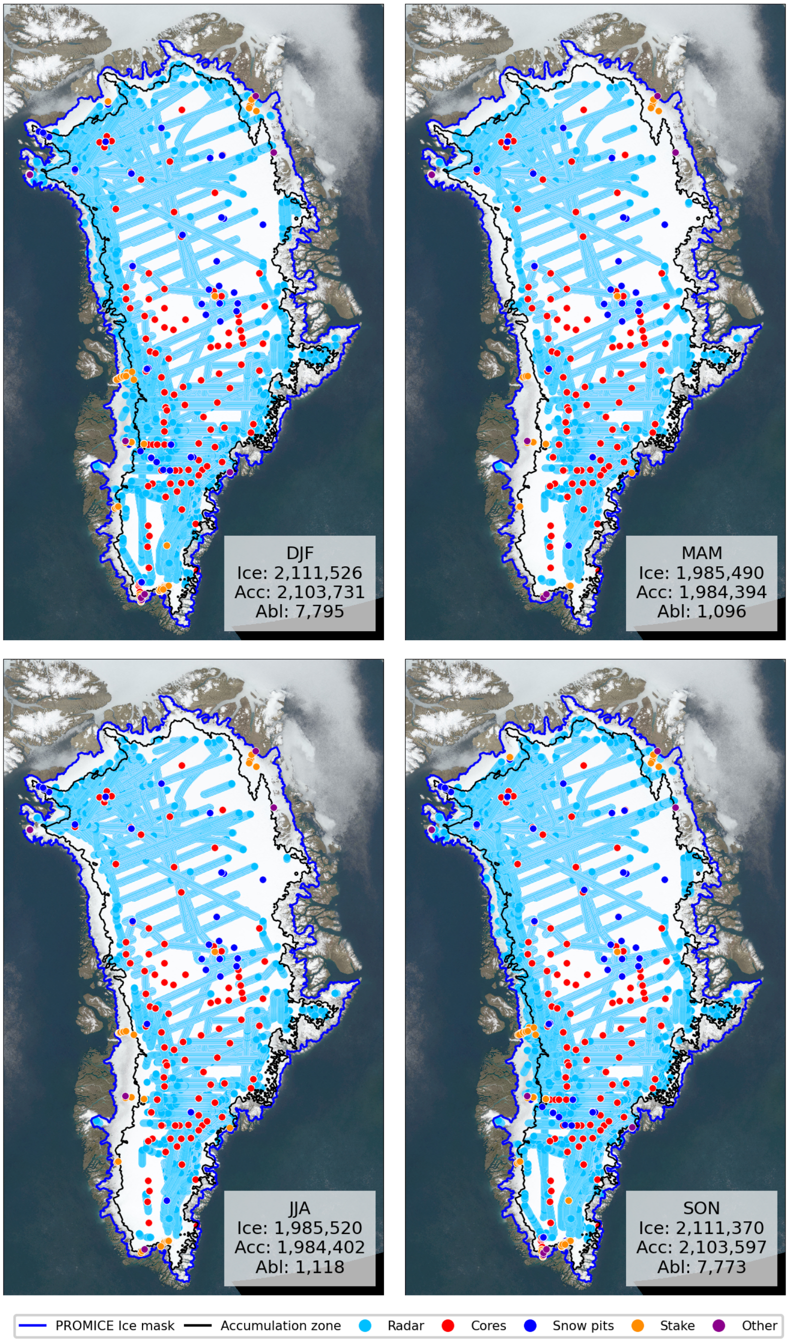

Figure A2. SUMup data distribution by season (1960-2022), illustrated by measurement type. The method type ‘other’ includes measurements from mass balance profile and SnowFox sensors. Values for ‘Ice’, ‘Acc’ and ‘Abl’ indicate the total number of data points for the ice-sheet, accumulation and ablation zones before radar grouping.

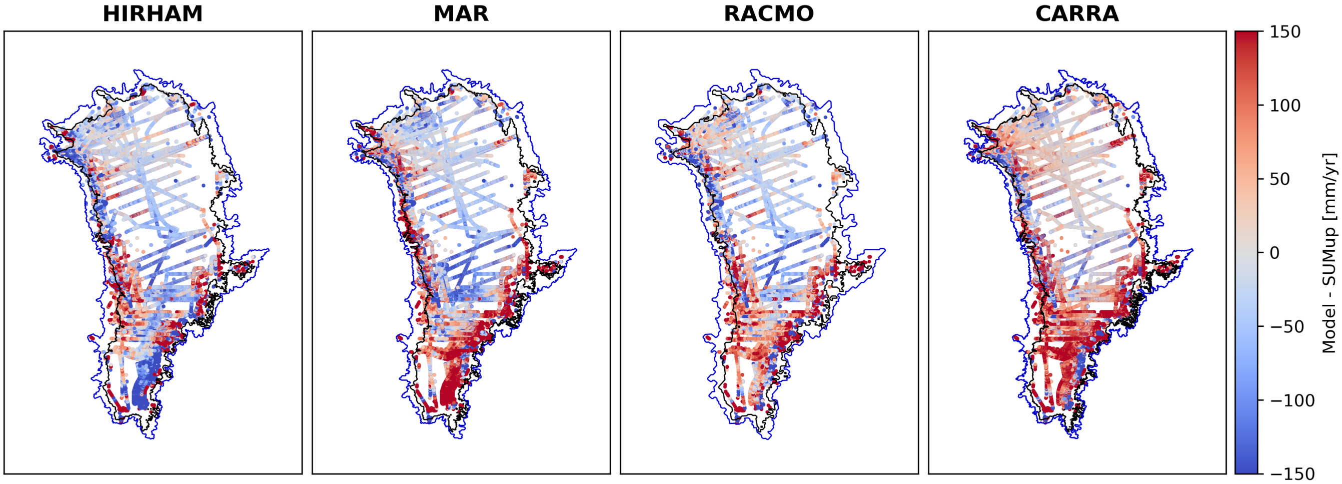

Figure A3. SUMup point-wise bias (1991-2022). The blue contour indicates the boundary of the PROMICE ice-sheet mask and the black contour shows the boundary of the accumulation zone.

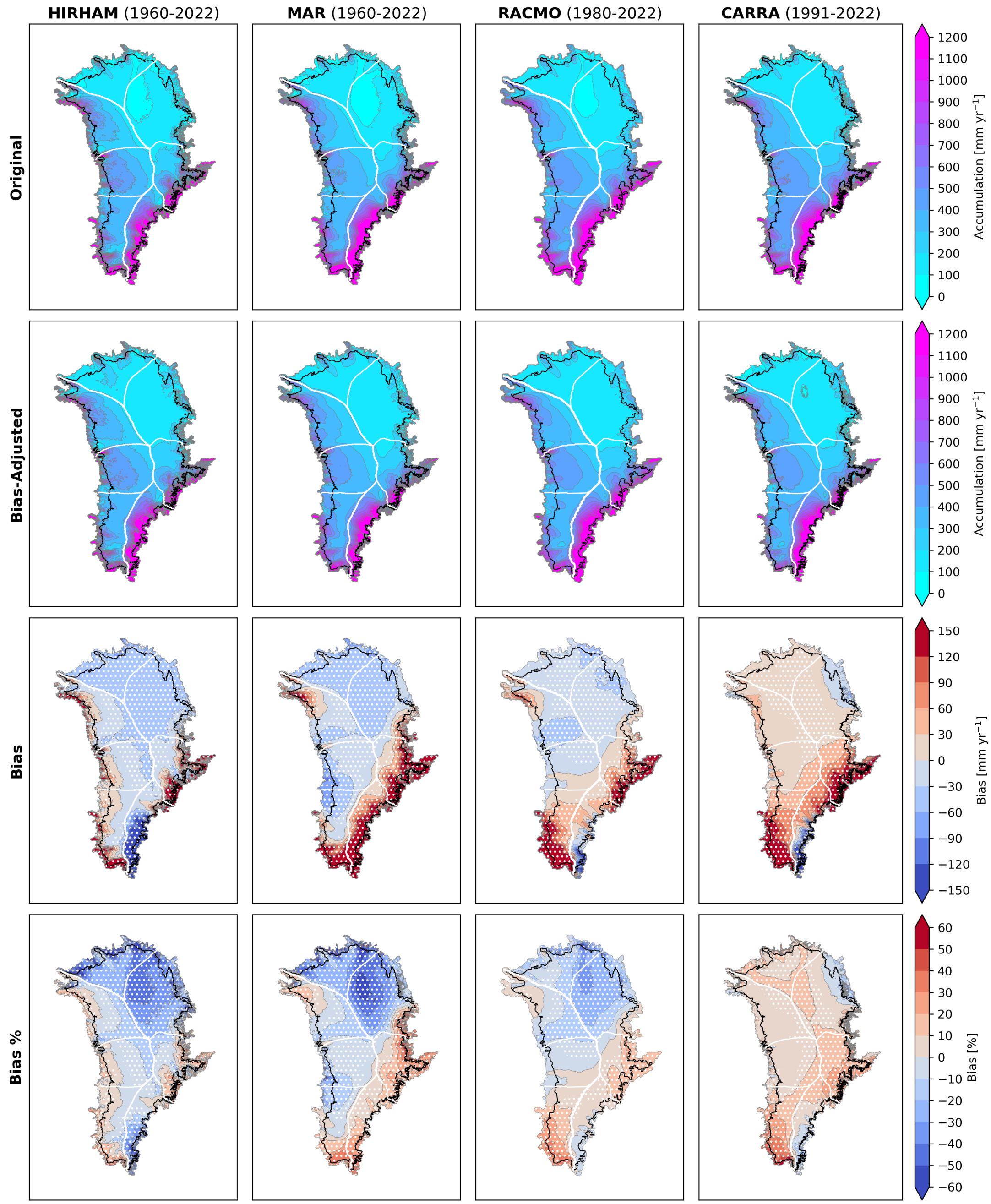

Figure A4. Mean maps of model accumulation and bias for the full model periods, HIRHAM (1960-2022), MAR (1960-2022), RACMO (1980-2022) and CARRA (1991-2022). The black line indicates the boundary of the accumulation zone. First row: original mean accumulation before adjustment. Second row: mean bias-corrected accumulation. Third row: mean bias in mm yr^{-1}. Fourth row: mean relative bias. Hatched regions indicate statistically significant biases ($p<0.05$). PROMICE drainage basin boundaries are indicated in white.

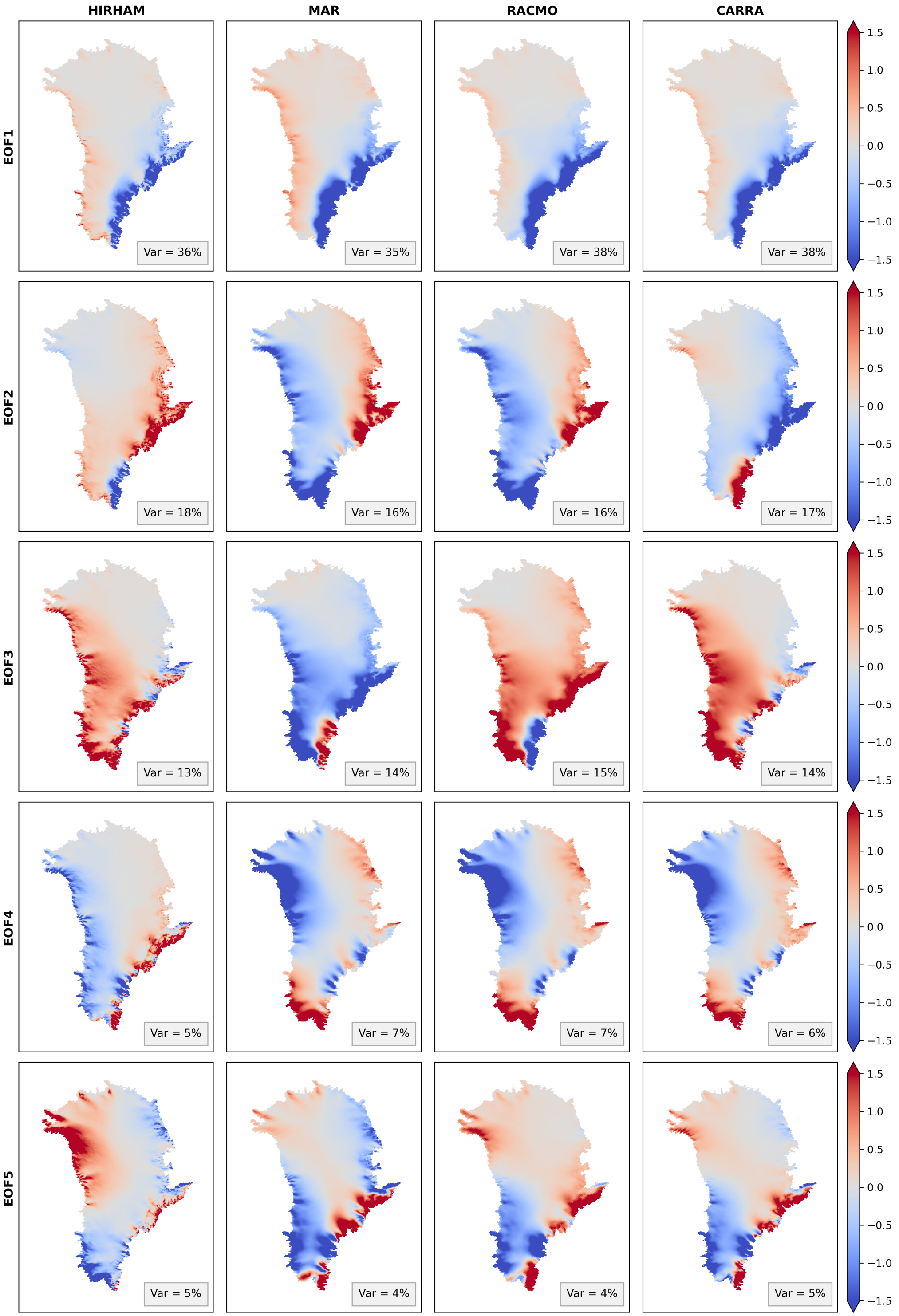

Figure A5. First five EOF patterns for HIRHAM, MAR, RACMO and CARRA over 1991-2022.

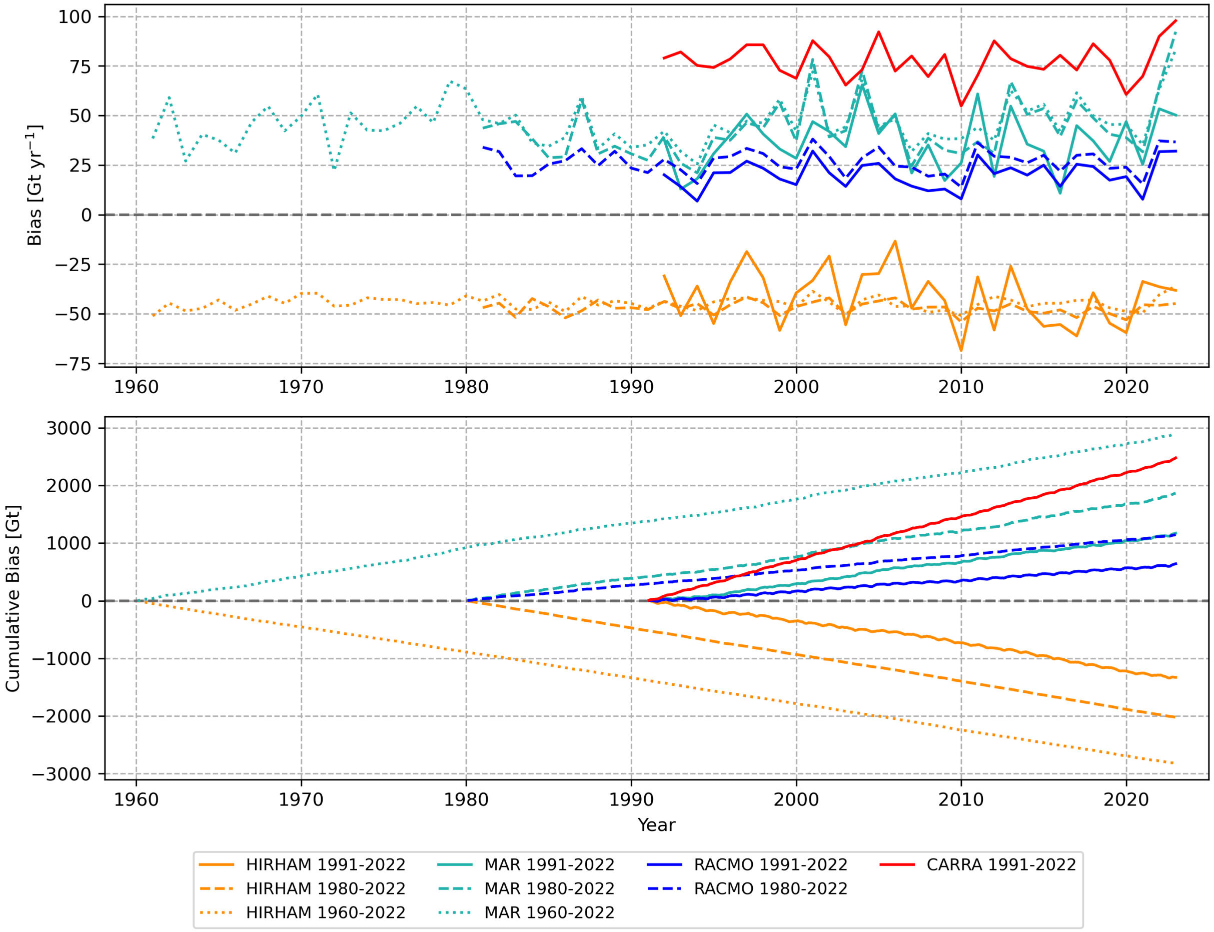

Figure A6. Spatially integrated annual bias for each model over the 1960-2022, 1980-2022 and 1991-2022 fitting periods, shown by year (upper) and as the cumulative sum (lower).

A1 Appendix Tables

		Ice Sheet			Accumulation Zone			Ablation Zone		
Period	**Model**	**Acc**	**Acc_{adj}** [Gt yr^{-1}]	**Bias**	**Acc**	**Acc_{adj}** [Gt yr^{-1}]	**Bias**	**Acc**	**Acc_{adj}** [Gt yr^{-1}]	**Bias**
1960–2022	HIRHAM	782	827 ± 48	$\mathbf{-45}$	514	555 ± 26	$\mathbf{-42}$	269	272 ± 23	-3
	MAR	754	708 ± 21	$\mathbf{+46}$	556	530 ± 13	$\mathbf{+26}$	199	178 ± 9	$\mathbf{+21}$
1980–2022	HIRHAM	795	842 ± 48	$\mathbf{-47}$	522	564 ± 23	$\mathbf{-43}$	274	278 ± 25	-4
	MAR	765	722 ± 19	$\mathbf{+43}$	562	538 ± 12	$\mathbf{+24}$	203	184 ± 8	$\mathbf{+19}$
	RACMO	809	783 ± 23	$\mathbf{+27}$	547	537 ± 13	$+10$	262	246 ± 11	$\mathbf{+17}$
1991–2022	HIRHAM	805	846 ± 43	$\mathbf{-42}$	528	571 ± 20	$\mathbf{-44}$	277	275 ± 23	$+2$
	MAR	779	742 ± 21	$\mathbf{+37}$	572	550 ± 13	$\mathbf{+21}$	207	192 ± 9	$\mathbf{+15}$
	RACMO	820	800 ± 19	$+20$	555	549 ± 10	$+6$	265	251 ± 9	$\mathbf{+14}$
	CARRA	808	730 ± 14	$\mathbf{+77}$	608	551 ± 8	$\mathbf{+56}$	200	179 ± 6	$\mathbf{+21}$

Table A1. Spatially integrated mean annual accumulation over the ice sheet, accumulation zone, and ablation zone expressed in Gt yr^{-1} for original (Acc) and bias-adjusted (Acc_{adj}) accumulation. Net bias is defined as Acc $-$ Acc_{adj}. Uncertainties for Acc_{adj} are obtained by eq. 10. Statistically significant biases based on the Monte Carlo AR(1) test ($p < 0.05$) are highlighted in bold.

		Basin-wise Bias [Gt yr^{-1}]						
Period	**Model**	**NO**	**NE**	**CE**	**SE**	**SW**	**CW**	**NW**
1960–2022	HIRHAM	$\mathbf{-11\ (-28\%)}$	$\mathbf{-15\ (-26\%)}$	$\mathbf{+17\ (+12\%)}$	$\mathbf{-48\ (-22\%)}$	$\mathbf{+12\ (+9\%)}$	$-1\ (-1\%)$	$+1\ (+1\%)$
	MAR	$\mathbf{-10\ (-27\%)}$	$\mathbf{-10\ (-17\%)}$	$\mathbf{+26\ (+20\%)}$	$\mathbf{+33\ (+16\%)}$	$\mathbf{+12\ (+9\%)}$	$\mathbf{-6\ (-8\%)}$	$0\ (0\%)$
1980–2022	HIRHAM	$\mathbf{-9\ (-24\%)}$	$\mathbf{-12\ (-19\%)}$	$\mathbf{+20\ (+14\%)}$	$\mathbf{-54\ (-25\%)}$	$\mathbf{+8\ (+6\%)}$	$-2\ (-2\%)$	$+2\ (+2\%)$
	MAR	$\mathbf{-12\ (-32\%)}$	$\mathbf{-7\ (-12\%)}$	$\mathbf{+27\ (+20\%)}$	$\mathbf{+32\ (+15\%)}$	$\mathbf{+12\ (+9\%)}$	$\mathbf{-7\ (-9\%)}$	$0\ (0\%)$
	RACMO	$\mathbf{-5\ (-12\%)}$	$\mathbf{-9\ (-14\%)}$	$\mathbf{+18\ (+12\%)}$	$+1\ (+1\%)$	$\mathbf{+26\ (+19\%)}$	$-3\ (-3\%)$	$-2\ (-2\%)$
1991–2022	HIRHAM	$\mathbf{-9\ (-23\%)}$	$-2\ (-2\%)$	$\mathbf{+20\ (+13\%)}$	$\mathbf{-39\ (-17\%)}$	$\mathbf{-13\ (-10\%)}$	$-2\ (-2\%)$	$+2\ (+2\%)$
	MAR	$\mathbf{-10\ (-28\%)}$	$\mathbf{-7\ (-11\%)}$	$\mathbf{+22\ (+16\%)}$	$\mathbf{+30\ (+14\%)}$	$\mathbf{+9\ (+6\%)}$	$\mathbf{-7\ (-9\%)}$	$+1\ (+1\%)$
	RACMO	$\mathbf{-4\ (-9\%)}$	$\mathbf{-9\ (-15\%)}$	$\mathbf{+18\ (+12\%)}$	$-1\ (-1\%)$	$\mathbf{+20\ (+14\%)}$	$-3\ (-3\%)$	$-1\ (0\%)$
	CARRA	$\mathbf{+4\ (+10\%)}$	$+3\ (+4\%)$	$\mathbf{+27\ (+20\%)}$	$-2\ (-1\%)$	$\mathbf{+34\ (+25\%)}$	$\mathbf{+6\ (+6\%)}$	$+5\ (+5\%)$

Table A2. Spatially integrated basin-wise accumulation net and relative bias expressed in Gt yr^{-1}. Bold values indicate statistically significant biases (p<0.05).

Period	Model	N	NE	CE	SE	SW	CW	NW
1960–2022	HIRHAM	0.9 / 0.8	7.7 / 7.8	25.8 / 26.0	17.3 / 18.0	5.4 / 5.5	2.8 / 2.7	2.1 / 1.6
	MAR	0.4 / 1.0	8.4 / 6.6	26.0 / 23.5	18.1 / 21.2	5.0 / 2.1	3.3 / 2.5	2.9 / 3.3
1980–2022	HIRHAM	-3.8 / -3.9	7.0 / 7.0	25.7 / 26.4	47.4 / 48.2	-1.5 / -1.3	-0.6 / -0.5	8.0 / 8.0
	MAR	-2.2 / -2.1	10.5 / 9.2	30.4 / 33.9	56.2 / 54.4	3.9 / -4.3	1.6 / -2.4	10.5 / 6.4
	RACMO	-2.4 / -3.1	10.5 / 7.8	22.5 / 23.1	45.2 / 46.1	0.1 / 1.3	1.7 / 1.2	7.7 / 5.4
1991–2022	HIRHAM	-5.6 / -5.8	7.8 / 7.8	30.5 / 34.9	57.7 / 65.7	-14.3 / -11.4	-4.2 / -1.9	4.5 / 5.4
	MAR	-3.1 / -4.2	14.1 / 14.6	34.4 / 33.5	66.0 / 64.2	-7.8 / -5.7	-1.6 / -3.0	5.2 / 0.5
	RACMO	-3.7 / -5.2	9.3 / 10.1	24.6 / 24.9	52.4 / 53.1	-13.4 / -10.7	-2.9 / -4.4	5.7 / 0.1
	CARRA	-2.5 / -6.1	10.5 / 10.2	14.9 / 21.5	34.2 / 36.1	-15.5 / -13.0	-8.0 / -6.1	6.0 / -0.8

Table A3. Basin-wise accumulation trends (mm yr^{-1}decade^{-1}) before (left) and after bias adjustment (right) for each model and evaluation period. Values for each basin are shown before (left) and after (right) bias adjustment.

Period	Model	N	NE	CE	SE	SW	CW	NW
1960–2022	HIRHAM	2.1 / 1.5	20.6 / 15.9	13.6 / 15.2	5.9 / 5.1	2.3 / 2.3	2.8 / 2.5	2.8 / 2.6
	MAR	1.4 / 2.3	21.8 / 15.3	14.4 / 18.1	6.8 / 9.3	1.7 / -1.3	2.6 / 1.7	2.9 / 3.4
1980–2022	HIRHAM	-5.5 / -4.3	12.6 / 10.8	9.0 / 10.3	7.4 / 5.6	-2.8 / -2.8	0.6 / 0.4	7.0 / 6.9
	MAR	-1.6 / -1.2	20.7 / 17.5	12.4 / 20.6	12.2 / 14.3	-0.5 / -4.7	1.7 / -1.4	9.8 / 5.7
	RACMO	-3.6 / -3.9	15.0 / 13.3	8.9 / 10.6	9.0 / 9.2	-0.8 / -0.6	2.4 / 1.9	6.1 / 4.3
1991–2022	HIRHAM	-9.3 / -7.6	7.8 / 7.2	8.5 / 11.9	9.0 / 8.1	-12.5 / -10.8	-2.2 / -1.2	4.1 / 4.7
	MAR	-2.6 / -3.4	20.2 / 22.3	11.6 / 16.5	14.4 / 15.8	-9.5 / -10.2	-1.5 / -4.3	4.9 / 0.0
	RACMO	-6.5 / -7.9	12.0 / 11.5	7.4 / 8.8	11.0 / 10.8	-10.0 / -11.4	-1.3 / -2.5	3.8 / 0.2
	CARRA	-4.1 / -9.4	9.9 / 14.2	1.3 / 8.1	5.4 / 5.4	-11.4 / -13.2	-4.6 / -4.2	5.1 / -0.3

Table A4. Basin-wise spatial mean accumulation sensitivity to temperature (% K^{-1}) for each model and evaluation period. Values for each basin are shown before (left) and after (right) bias adjustment.

Author contributions. JLC and AG designed the bias-adjustment method. BV provided the figure of model evaluation against the 6 individual ice core sites. JLC wrote the initial manuscript, prepared and filtered the SUMup dataset, and created the remaining figures and tables. All authors participated in the data interpretation and commented on the paper.

Competing interests. No competing interests are present.

Acknowledgements. JLC, AG and CH received funding from the Novo Nordisk Foundation (NNF Challenge, PRECISE – Prediction of Ice Sheets on Earth, grant no. NNF23OC0081251). CH received funding from the European Union (Horizon Europe, ICELINK, grant no. 101184621). The authors thank Martin Olesen (Danish Meteorological Institute) for providing HIRHAM5 data (1960-2022), Kristiina Verro (Danish Meteorological Institute) for providing RACMO data (1980-2022), and Clément Cherblanc for valuable feedback on the manuscript. The SUMup 2024 dataset was supported by PROMICE.

References

Bales, R. C., Guo, Q., Shen, D., McConnell, J. R., Du, G., Burkhart, J. F., Spikes, V. B., Hanna, E., and Cappelen, J.: Annual accumulation for Greenland updated using ice core data developed during 2000–2006 and analysis of daily coastal meteorological data, Journal of Geophysical Research: Atmospheres, 114, https://doi.org/10.1029/2008JD011208, 2009.

Banta, J. R. and McConnell, J. R.: Annual accumulation over recent centuries at four sites in central Greenland, Journal of Geophysical Research: Atmospheres, 112, https://doi.org/10.1029/2006JD007887, 2007.

Batrak, Y., Cheng, B., and Kallio-Myers, V.: Sea ice cover in the Copernicus Arctic Regional Reanalysis, The Cryosphere, 18, 1157–1183, https://doi.org/10.5194/tc-18-1157-2024, publisher: Copernicus GmbH, 2024.

Bengtsson, L., Andrae, U., Aspelien, T., Batrak, Y., Calvo, J., Rooy, W. d., Gleeson, E., Hansen-Sass, B., Homleid, M., Hortal, M., Ivarsson, K.-I., Lenderink, G., Niemelä, S., Nielsen, K. P., Onvlee, J., Rontu, L., Samuelsson, P., Muñoz, D. S., Subias, A., Tijm, S., Toll, V., Yang, X., and Køltzow, M. : The HARMONIE–AROME Model Configuration in the ALADIN–HIRLAM NWP System, https://doi.org/10.1175/MWR-D-16-0417.1, section: Monthly Weather Review, 2017.

Bennartz, R., Fell, F., Pettersen, C., Shupe, M. D., and Schuettemeyer, D.: Spatial and temporal variability of snowfall over Greenland from CloudSat observations, Atmospheric Chemistry and Physics, 19, 8101–8121, https://doi.org/10.5194/acp-19-8101-2019, 2019.

Bingham, R. G., Bodart, J. A., Cavitte, M. G. P., Chung, A., Sanderson, R. J., Sutter, J. C. R., Eisen, O., Karlsson, N. B., MacGregor, J. A., Ross, N., Young, D. A., Ashmore, D. W., Born, A., Chu, W., Cui, X., Drews, R., Franke, S., Goel, V., Goodge, J. W., Henry, A. C. J., Hermant, A., Hills, B. H., Holschuh, N., Koutnik, M. R., Leysinger Vieli, G. J.-M. C., MacKie, E. J., Mantelli, E., Martín, C., Ng, F. S. L., Oraschewski, F. M., Napoleoni, F., Parrenin, F., Popov, S. V., Rieckh, T., Schlegel, R., Schroeder, D. M., Siegert, M. J., Tang, X., Teisberg, T. O., Winter, K., Yan, S., Davis, H., Dow, C. F., Fudge, T. J., Jordan, T. A., Kulessa, B., Matsuoka, K., Nyqvist, C. J., Rahnemoonfar, M., Siegfried, M. R., Singh, S., Višnjević, V., Zamora, R., and Zuhr, A.: Review article: AntArchitecture – building an age–depth model from Antarctica's radiostratigraphy to explore ice-sheet evolution, The Cryosphere, 19, 4611–4655, https://doi.org/10.5194/tc-19-4611-2025, publisher: Copernicus GmbH, 2025.

Bochow, N., Poltronieri, A., and Boers, N.: Projections of precipitation and temperatures in Greenland and the impact of spatially uniform anomalies on the evolution of the ice sheet, The Cryosphere, 18, 5825–5863, https://doi.org/10.5194/tc-18-5825-2024, 2024.

Bolzan, J. F. and Strobel, M.: Accumulation-rate variations around Summit, Greenland, Journal of Glaciology, 40, 56–66, https://doi.org/10.3189/s0022143000003798, 1994.

Bolzan, J. F. and Strobel, M.: Oxygen isotope data from snowpit at GISP2 Site 13, PANGAEA, https://doi.org/10.1594/PANGAEA.55510, 1999a.

Bolzan, J. F. and Strobel, M.: Oxygen isotope data from snowpit at GISP2 Site 15, PANGAEA, https://doi.org/10.1594/PANGAEA.55511, 1999b.

Bolzan, J. F. and Strobel, M.: Oxygen isotope data from snowpit at GISP2 Site 31, PANGAEA, https://doi.org/10.1594/PANGAEA.55512, 1999c.

Bolzan, J. F. and Strobel, M.: Oxygen isotope data from snowpit at GISP2 Site 37, PANGAEA, https://doi.org/10.1594/PANGAEA.55513, 1999d.

Bolzan, J. F. and Strobel, M.: Oxygen isotope data from snowpit at GISP2 Site 51, PANGAEA, https://doi.org/10.1594/PANGAEA.55514, 1999e.

Bolzan, J. F. and Strobel, M.: Oxygen isotope data from snowpit at GISP2 Site 57, PANGAEA, https://doi.org/10.1594/PANGAEA.55515, 1999f.

Bolzan, J. F. and Strobel, M.: Oxygen isotope data from snowpit at GISP2 Site 73, PANGAEA, https://doi.org/10.1594/PANGAEA.55516, 1999g.

Bolzan, J. F. and Strobel, M.: Oxygen isotope data from snowpit at GISP2 Site 44, PANGAEA, https://doi.org/10.1594/PANGAEA.59995, 2001a.

Bolzan, J. F. and Strobel, M.: Oxygen isotope data from snowpit at GISP2 Site 571, PANGAEA, https://doi.org/10.1594/PANGAEA.59996, 2001b.

Box, J. E.: Greenland ice sheet surface mass-balance variability: 1991–2003, Annals of Glaciology, 42, 90–94, https://doi.org/10.3189/172756405781812772, 2005.

Box, J. E., Bromwich, D. H., and Bai, L.-S.: Greenland ice sheet surface mass balance 1991–2000: Application of Polar MM5 mesoscale model and in situ data, Journal of Geophysical Research: Atmospheres, 109, https://doi.org/10.1029/2003JD004451, 2004.

Box, J. E., Bromwich, D. H., Veenhuis, B. A., Bai, L.-S., Stroeve, J. C., Rogers, J. C., Steffen, K., Haran, T., and Wang, S.-H.: Greenland Ice Sheet Surface Mass Balance Variability (1988–2004) from Calibrated Polar MM5 Output, https://doi.org/10.1175/JCLI3738.1, 2006.

Box, J. E., Yang, L., Bromwich, D. H., and Bai, L.-S.: Greenland Ice Sheet Surface Air Temperature Variability: 1840–2007, https://doi.org/10.1175/2009JCLI2816.1, 2009.

Box, J. E., Cressie, N., Bromwich, D. H., Jung, J.-H., Broeke, M. v. d., Angelen, J. H. v., Forster, R. R., Miège, C., Mosley-Thompson, E., Vinther, B., and McConnell, J. R.: Greenland Ice Sheet Mass Balance Reconstruction. Part I: Net Snow Accumulation (1600–2009), https://doi.org/10.1175/JCLI-D-12-00373.1, 2013.

Box, J. E., Nielsen, K. P., Yang, X., Niwano, M., Wehrlé, A., van As, D., Fettweis, X., Køltzow, M. A. , Palmason, B., Fausto, R. S., van den Broeke, M. R., Huai, B., Ahlstrøm, A. P., Langley, K., Dachauer, A., and Noël, B.: Greenland ice sheet rainfall climatology, extremes and atmospheric river rapids, Meteorological Applications, 30, e2134, https://doi.org/10.1002/met.2134, 2023.

Brun, E., David, P., Sudul, M., and Brunot, G.: A numerical model to simulate snow-cover stratigraphy for operational avalanche forecasting, Journal of Glaciology, 38, 13–22, https://doi.org/10.3189/S0022143000009552, 1992.

Buchardt, S. L., Clausen, H. B., Vinther, B. M., and Dahl-Jensen, D.: Investigating the past and recent δ^{18}O-accumulation relationship seen in Greenland ice cores, Climate of the Past, 8, 2053–2059, https://doi.org/10.5194/cp-8-2053-2012, 2012.

Burgess, E. W., Forster, R. R., Box, J. E., Mosley-Thompson, E., Bromwich, D. H., Bales, R. C., and Smith, L. C.: A spatially calibrated model of annual accumulation rate on the Greenland Ice Sheet (1958–2007), Journal of Geophysical Research: Earth Surface, 115, https://doi.org/10.1029/2009JF001293, 2010.

Calanca, P., Gilgen, H., Ekholm, S., and Ohmura, A.: Gridded temperature and accumulation distributions for Greenland for use in cryospheric models, Annals of Glaciology, 31, 118–120, https://doi.org/10.3189/172756400781820345, 2000.

Chandler, D. M., Alcock, J. D., Wadham, J. L., Mackie, S. L., and Telling, J.: Seasonal changes of ice surface characteristics and productivity in the ablation zone of the Greenland Ice Sheet, The Cryosphere, 9, 487–504, https://doi.org/10.5194/tc-9-487-2015, 2015.

Chandler, D. M., Wadham, J. L., Nienow, P. W., Doyle, S. H., Tedstone, A. J., Telling, J., Hawkings, J., Alcock, J. D., Linhoff, B., and Hubbard, A.: Rapid development and persistence of efficient subglacial drainage under 900 m-thick ice in Greenland, Earth and Planetary Science Letters, 566, 116 982, https://doi.org/10.1016/j.epsl.2021.116982, 2021.

Chen, X., Zhang, X., Church, J. A., Watson, C. S., King, M. A., Monselesan, D., Legresy, B., and Harig, C.: The increasing rate of global mean sea-level rise during 1993–2014, Nature Climate Change, 7, 492–495, https://doi.org/10.1038/nclimate3325, publisher: Nature Publishing Group, 2017.

Clapeyron, : Mémoire sur la puissance motrice de la chaleur, J. Gabay, Paris, [reproduction en fac-similé] edn., ISBN 978-2-87647-283-9, http://catalogue.bnf.fr/ark:/12148/cb40936143n, 2006.

Clausen, H., Gundestrup, N., Johnsen, S., Bindschadler, R., and Zwally, J.: Glaciological Investigations in the Crête Area, Central Greenland: A Search for a new Deep-Drilling Site, Annals of Glaciology, 10, 10–15, https://doi.org/10.3189/s0260305500004080, 1988.

Clausius, R.: Ueber die bewegende Kraft der Wärme und die Gesetze, welche sich daraus für die Wärmelehre selbst ableiten lassen, Annalen der Physik, 155, 368–397, https://doi.org/10.1002/andp.18501550306, 1850.

Cogley, J. G.: Greenland accumulation: An error model, Journal of Geophysical Research: Atmospheres, 109, https://doi.org/10.1029/2003JD004449, 2004.

Copernicus Climate Change Service: CARRA User Guide, Tech. rep., European Centre for Medium-Range Weather Forecasts, https://climate.copernicus.eu/copernicus-arctic-regional-reanalysis-carra, 2021.

Dawson, A.: eofs: A Library for EOF Analysis of Meteorological, Oceanographic, and Climate Data, Journal of Open Research Software, 4, https://doi.org/10.5334/jors.122, 2016.

Delhasse, A., Kittel, C., Amory, C., Hofer, S., van As, D., S. Fausto, R., and Fettweis, X.: Brief communication: Evaluation of the near-surface climate in ERA5 over the Greenland Ice Sheet, The Cryosphere, 14, 957–965, https://doi.org/10.5194/tc-14-957-2020, publisher: Copernicus GmbH, 2020.

Dibb, J. E. and Fahnestock, M.: Snow accumulation, surface height change, and firn densification at Summit, Greenland: Insights from 2 years of in situ observation, Journal of Geophysical Research: Atmospheres, 109, https://doi.org/10.1029/2003jd004300, 2004.

DMI, Christensen, B., and Christensen, H.: The HIRHAM Regional Climate Model. Version 5 (beta), Technical Report, 2017.

Ettema, J., van den Broeke, M. R., van Meijgaard, E., van de Berg, W. J., Bamber, J. L., Box, J. E., and Bales, R. C.: Higher surface mass balance of the Greenland ice sheet revealed by high-resolution climate modeling, Geophysical Research Letters, 36, https://doi.org/10.1029/2009GL038110, 2009.

Ettema, J., van den Broeke, M. R., van Meijgaard, E., van de Berg, W. J., Box, J. E., and Steffen, K.: Climate of the Greenland ice sheet using a high-resolution climate model – Part 1: Evaluation, The Cryosphere, 4, 511–527, https://doi.org/10.5194/tc-4-511-2010, publisher: Copernicus GmbH, 2010.

Fausto, R. S.: Snow-water equivalent of snowpacks, GEUS Dataverse, N/A, N/A, https://doi.org/10.22008/FK2/B5KVJV, 2021.

Fausto, R. S., Andersen, S. B., Ahlstrøm, A. P., van As, D., Box, J. E., Binder, D., Citterio, M., Colgan, W., Haubner, K., Hansen, K., Karlsson, N. B., Mankoff, K. D., Pedersen, A. , Solgaard, A., and Vandecrux, B.: Greenland ice sheet – snowline elevations at the end of the melt seasons from 2000 to 2017, Geological Survey of Denmark and Greenland Bulletin, 41, 71–74, 2018.

Fausto, R. S., van As, D., Mankoff, K. D., Vandecrux, B., Citterio, M., Ahlstrøm, A. P., Andersen, S. B., Colgan, W., Karlsson, N. B., Kjeldsen, K. K., Korsgaard, N. J., Larsen, S. H., Nielsen, S., Pedersen, A. , Shields, C. L., Solgaard, A. M., and Box, J. E.: Programme for Monitoring of the Greenland Ice Sheet (PROMICE) automatic weather station data, Earth System Science Data, 13, 3819–3845, https://doi.org/10.5194/essd-13-3819-2021, 2021.

Fettweis, X. and Grailet, J.-F.: MAR (Modèle Atmosphérique Régional) version 3.14, https://doi.org/10.5281/ZENODO.13151274, language: en, 2024.

Fettweis, X., Hanna, E., Gallée, H., Huybrechts, P., and Erpicum, M.: Estimation of the Greenland ice sheet surface mass balance for the 20th and 21st centuries, The Cryosphere, 2, 117–129, https://doi.org/10.5194/tc-2-117-2008, 2008.

Fettweis, X., Tedesco, M., van den Broeke, M., and Ettema, J.: Melting trends over the Greenland ice sheet (1958–2009) from spaceborne microwave data and regional climate models, The Cryosphere, 5, 359–375, https://doi.org/10.5194/tc-5-359-2011, publisher: Copernicus GmbH, 2011.

Fettweis, X., Hofer, S., Krebs-Kanzow, U., Amory, C., Aoki, T., Berends, C. J., Born, A., Box, J. E., Delhasse, A., Fujita, K., Gierz, P., Goelzer, H., Hanna, E., Hashimoto, A., Huybrechts, P., Kapsch, M.-L., King, M. D., Kittel, C., Lang, C., Langen, P. L., Lenaerts, J. T. M., Liston, G. E., Lohmann, G., Mernild, S. H., Mikolajewicz, U., Modali, K., Mottram, R. H., Niwano, M., Noël, B., Ryan, J. C., Smith, A., Streffing, J., Tedesco, M., van de Berg, W. J., van den Broeke, M., van de Wal, R. S. W., van Kampenhout, L., Wilton, D., Wouters, B., Ziemen, F., and Zolles, T.: GrSMBMIP: intercomparison of the modelled 1980–2012 surface mass balance over the Greenland Ice Sheet, The Cryosphere, 14, 3935–3958, https://doi.org/10.5194/tc-14-3935-2020, publisher: Copernicus GmbH, 2020.

Freitag, J., Kipfstuhl, S., Weißbach, S., Karlsson, N. B., Münch, T., and Hörhold, M.: Accumulation rate of the NG2012 firn core, PANGAEA, https://doi.org/10.1594/PANGAEA.944514, 2022a.

Freitag, J., Kipfstuhl, S., Weißbach, S., Karlsson, N. B., Münch, T., and Hörhold, M.: Accumulation rate of the B23_2012 firn core, PANGAEA, https://doi.org/10.1594/PANGAEA.944513, 2022b.

Freitag, J., Kipfstuhl, S., Weißbach, S., Karlsson, N. B., Münch, T., and Hörhold, M.: Accumulation rate of the B18_2012 firn core, PANGAEA, https://doi.org/10.1594/PANGAEA.944454, 2022c.

Gallée, H. and Schayes, G.: Development of a Three-Dimensional Meso-γ Primitive Equation Model: Katabatic Winds Simulation in the Area of Terra Nova Bay, Antarctica, Monthly Weather Review, 122, 671–685, https://doi.org/10.1175/1520-0493(1994)122<0671:DOATDM>2.0.CO;2, publisher: American Meteorological Society Section: Monthly Weather Review, 1994.

Graeter, K. A., Osterberg, E. C., Ferris, D. G., Hawley, R. L., Marshall, H. P., Lewis, G., Meehan, T., McCarthy, F., Overly, T., and Birkel, S. D.: Ice Core Records of West Greenland Melt and Climate Forcing, Geophysical Research Letters, 45, 3164–3172, https://doi.org/10.1002/2017gl076641, 2018.

Haacker, J., Wouters, B., Fettweis, X., Glissenaar, I. A., and Box, J. E.: Atmospheric-river-induced foehn events drain glaciers on Novaya Zemlya, Nature Communications, 15, 7021, https://doi.org/10.1038/s41467-024-51404-8, publisher: Nature Publishing Group, 2024.

Hammer, C. U. and Dahl-Jensen, D.: GRIP Accumulation Rates, PANGAEA, https://doi.org/10.1594/PANGAEA.55084, 1999.

Hanna, E., Huybrechts, P., Janssens, I., Cappelen, J., Steffen, K., and Stephens, A.: Runoff and mass balance of the Greenland ice sheet: 1958–2003, Journal of Geophysical Research: Atmospheres, 110, https://doi.org/10.1029/2004JD005641, 2005.

Hanna, E., McConnell, J., Das, S., Cappelen, J., and Stephens, A.: Observed and Modeled Greenland Ice Sheet Snow Accumulation, 1958–2003, and Links with Regional Climate Forcing, Journal of Climate, 19, 344–358, https://doi.org/10.1175/jcli3615.1, 2006.

Hanna, E., Huybrechts, P., Steffen, K., Cappelen, J., Huff, R., Shuman, C., Irvine-Fynn, T., Wise, S., and Griffiths, M.: Increased Runoff from Melt from the Greenland Ice Sheet: A Response to Global Warming, https://doi.org/10.1175/2007JCLI1964.1, 2008.

Hanna, E., Huybrechts, P., Cappelen, J., Steffen, K., Bales, R. C., Burgess, E., McConnell, J. R., Peder Steffensen, J., Van Den Broeke, M., Wake, L., Bigg, G., Griffiths, M., and Savas, D.: Greenland Ice Sheet surface mass balance 1870 to 2010 based on Twentieth Century Reanalysis, and links with global climate forcing: GREENLAND ICE SHEET MASS BALANCE, Journal of Geophysical Research: Atmospheres, 116, https://doi.org/10.1029/2011JD016387, 2011.

Hanna, E., Topál, D., Box, J. E., Buzzard, S., Christie, F. D. W., Hvidberg, C., Morlighem, M., De Santis, L., Silvano, A., Colleoni, F., Sasgen, I., Banwell, A. F., van den Broeke, M. R., DeConto, R., De Rydt, J., Goelzer, H., Gossart, A., Gudmundsson, G. H., Lindbäck, K., Miles, B., Mottram, R., Pattyn, F., Reese, R., Rignot, E., Srivastava, A., Sun, S., Toller, J., Tuckett, P. A., and Ultee, L.: Short- and long-term variability of the Antarctic and Greenland ice sheets, Nature Reviews Earth & Environment, 5, 193–210, https://doi.org/10.1038/s43017-023-00509-7, 2024.

Hawley, R. L., Courville, Z. R., Kehrl, L. M., Lutz, E. R., Osterberg, E. C., Overly, T. B., and Wong, G. J.: Recent accumulation variability in northwest Greenland from ground-penetrating radar and shallow cores along the Greenland Inland Traverse, Journal of Glaciology, 60, 375–382, https://doi.org/10.3189/2014jog13j141, 2014.

Hermann, M., Box, J. E., Fausto, R. S., Colgan, W. T., Langen, P. L., Mottram, R., Wuite, J., Noël, B., van den Broeke, M. R., and van As, D.: Application of PROMICE Q-Transect in Situ Accumulation and Ablation Measurements (2000–2017) to Constrain Mass Balance at the Southern Tip of the Greenland Ice Sheet, Journal of Geophysical Research: Earth Surface, 123, 1235–1256, https://doi.org/10.1029/2017JF004408, 2018.

Hersbach, H., Bell, W., Berrisford, P., Horányi, A., J., M.-S., Nicolas, J., Radu, R., Schepers, D., Simmons, A., Soci, C., and Dee, D.: Global reanalysis: goodbye ERA-Interim, hello ERA5, https://doi.org/10.21957/VF291HEHD7, publisher: ECMWF, 2019.

Hersbach, H., Bell, B., Berrisford, P., Hirahara, S., Horányi, A., Muñoz-Sabater, J., Nicolas, J., Peubey, C., Radu, R., Schepers, D., Simmons, A., Soci, C., Abdalla, S., Abellan, X., Balsamo, G., Bechtold, P., Biavati, G., Bidlot, J., Bonavita, M., De Chiara, G., Dahlgren, P., Dee, D., Diamantakis, M., Dragani, R., Flemming, J., Forbes, R., Fuentes, M., Geer, A., Haimberger, L., Healy, S., Hogan, R. J., Hólm, E., Janisková, M., Keeley, S., Laloyaux, P., Lopez, P., Lupu, C., Radnoti, G., de Rosnay, P., Rozum, I., Vamborg, F., Villaume, S., and Thépaut, J.-N.: The ERA5 global reanalysis, Quarterly Journal of the Royal Meteorological Society, 146, 1999–2049, https://doi.org/10.1002/qj.3803, _eprint: https://rmets.onlinelibrary.wiley.com/doi/pdf/10.1002/qj.3803, 2020.

Hofer, S., Lang, C., Amory, C., Kittel, C., Delhasse, A., Tedstone, A., and Fettweis, X.: Greater Greenland Ice Sheet contribution to global sea level rise in CMIP6, Nature Communications, 11, 6289, https://doi.org/10.1038/s41467-020-20011-8, 2020.

Howat, I. M., de la Peña, S., Desilets, D., and Womack, G.: Autonomous ice sheet surface mass balance measurements from cosmic rays, The Cryosphere, 12, 2099–2108, https://doi.org/10.5194/tc-12-2099-2018, 2018.

Huai, B., van den Broeke, M. R., Reijmer, C. H., and Noël, B.: A Daily 1-km Resolution Greenland Rainfall Climatology (1958–2020) From Statistical Downscaling of a Regional Atmospheric Climate Model, Journal of Geophysical Research: Atmospheres, 127, e2022JD036 688, https://doi.org/10.1029/2022JD036688, _eprint: https://agupubs.onlinelibrary.wiley.com/doi/pdf/10.1029/2022JD036688, 2022.

Intergovernmental Panel On Climate Change, ed.: Climate Change 2013 – The Physical Science Basis: Working Group I Contribution to the Fifth Assessment Report of the Intergovernmental Panel on Climate Change, Cambridge University Press, 1 edn., ISBN 978-1-107-05799-9 978-1-107-66182-0 978-1-107-41532-4, https://www.cambridge.org/core/product/identifier/9781107415324/type/book, 2014.

Isaksen, K., Nordli, , Ivanov, B., Køltzow, M. A. , Aaboe, S., Gjelten, H. M., Mezghani, A., Eastwood, S., Førland, E., Benestad, R. E., Hanssen-Bauer, I., Brækkan, R., Sviashchennikov, P., Demin, V., Revina, A., and Karandasheva, T.: Exceptional warming over the Barents area, Scientific Reports, 12, 9371, https://doi.org/10.1038/s41598-022-13568-5, publisher: Nature Publishing Group, 2022.

Jia, Y., Xiao, K., Lin, M., and Zhang, X.: Analysis of Global Sea Level Change Based on Multi-Source Data, Remote Sensing, 14, 4854, https://doi.org/10.3390/rs14194854, 2022.

Kawakami, K., Iizuka, Y., Sasage, M., Matsumoto, M., Saito, T., Hori, A., Ishino, S., Fujita, S., Fujita, K., Takasugi, K., Hatakeyama, T., Hamamoto, S., Watari, A., Esashi, N., Otsuka, M., Uemura, R., Horiuchi, K., Minowa, M., Hattori, S., Aoki, T., Hirabayashi, M., Kawamura, K., and Matoba, S.: SE-Dome II Ice Core Dating With Half-Year Precision: Increasing Melting Events From 1799 to 2020 in Southeastern Greenland, Journal of Geophysical Research: Atmospheres, 128, https://doi.org/10.1029/2023jd038874, 2023.

Khan, S. A., Aschwanden, A., Bjørk, A. A., Wahr, J., Kjeldsen, K. K., and Kjær, K. H.: Greenland ice sheet mass balance: a review, Reports on Progress in Physics, 78, 046 801, https://doi.org/10.1088/0034-4885/78/4/046801, 2015.

Kjær, H., Zens, P., Edwards, R., Olesen, M., Mottram, R., Lewis, G., Holme, C., Black, S., Lund, K., Schmidt, M., Dahl-Jensen, D., Vinther, B., Svensson, A., Karlsson, N., Box, J., Kipfstuhl, S., and Vallelonga, P.: Recent North Greenland temperature warming and accumulation, 2021.

Koenig, L. S., Ivanoff, A., Alexander, P. M., MacGregor, J. A., Fettweis, X., Panzer, B., Paden, J. D., Forster, R. R., Das, I., McConnell, J. R., Tedesco, M., Leuschen, C., and Gogineni, P.: Annual Greenland accumulation rates (2009–2012) from airborne snow radar, The Cryosphere, 10, 1739–1752, https://doi.org/10.5194/tc-10-1739-2016, 2016.

Kokhanovsky, A., Vandecrux, B., Wehrlé, A., Danne, O., Brockmann, C., and Box, J. E.: An Improved Retrieval of Snow and Ice Properties Using Spaceborne OLCI/S-3 Spectral Reflectance Measurements: Updated Atmospheric Correction and Snow Impurity Load Estimation, Remote Sensing, 15, 77, https://doi.org/10.3390/rs15010077, publisher: Multidisciplinary Digital Publishing Institute, 2023.

Køltzow, M., Schyberg, H., Støylen, E., and Yang, X.: Value of the Copernicus Arctic Regional Reanalysis (CARRA) in representing near-surface temperature and wind speed in the north-east European Arctic, Polar Research, 41, https://doi.org/10.33265/polar.v41.8002, 2022.

Langen, P. L., Mottram, R. H., Christensen, J. H., Boberg, F., Rodehacke, C. B., Stendel, M., As, D. v., Ahlstrøm, A. P., Mortensen, J., Rysgaard, S., Petersen, D., Svendsen, K. H., Aðalgeirsdóttir, G., and Cappelen, J.: Quantifying Energy and Mass Fluxes Controlling Godthåbsfjord Freshwater Input in a 5-km Simulation (1991–2012), https://doi.org/10.1175/JCLI-D-14-00271.1, 2015.

Langen, P. L., Fausto, R. S., Vandecrux, B., Mottram, R. H., and Box, J. E.: Liquid Water Flow and Retention on the Greenland Ice Sheet in the Regional Climate Model HIRHAM5: Local and Large-Scale Impacts, Frontiers in Earth Science, 4, https://doi.org/10.3389/feart.2016.00110, 2017.

Lenssen, N., Schmidt, G. A., Hendrickson, M., Jacobs, P., Menne, M. J., and Ruedy, R.: A NASA GISTEMPv4 Observational Uncertainty Ensemble, Journal of Geophysical Research: Atmospheres, 129, e2023JD040 179, https://doi.org/10.1029/2023JD040179, _eprint: https://agupubs.onlinelibrary.wiley.com/doi/pdf/10.1029/2023JD040179, 2024.

Lewis, G., Osterberg, E., Hawley, R., Whitmore, B., Marshall, H. P., and Box, J.: Regional Greenland accumulation variability from Operation IceBridge airborne accumulation radar, The Cryosphere, 11, 773–788, https://doi.org/10.5194/tc-11-773-2017, 2017.

Lewis, G., Osterberg, E., Hawley, R., Marshall, H. P., Meehan, T., Graeter, K., McCarthy, F., Overly, T., Thundercloud, Z., and Ferris, D.: Recent precipitation decrease across the western Greenland ice sheet percolation zone, The Cryosphere, 13, 2797–2815, https://doi.org/10.5194/tc-13-2797-2019, 2019.

Lucas-Picher, P., Wulff-Nielsen, M., Christensen, J. H., Aðalgeirsdóttir, G., Mottram, R., and Simonsen, S. B.: Very high resolution regional climate model simulations over Greenland: Identifying added value, Journal of Geophysical Research: Atmospheres, 117, https://doi.org/10.1029/2011JD016267, 2012.

Luetzenburg, G., Korsgaard, N. J., Deichmann, A. K., Socher, T., Gleie, K., Scharffenberger, T., Meyer, R. P., Fahrner, D., Nielsen, E. B., How, P., Bjørk, A. A., Kjeldsen, K. K., Ahlstrøm, A. P., and Fausto, R. S.: PROMICE-2022 Ice Mask: A high-resolution outline of the Greenland Ice Sheet from August 2022, Earth System Science Data Discussions, pp. 1–23, https://doi.org/10.5194/essd-2025-415, publisher: Copernicus GmbH, 2025.

Machguth, H., MacFerrin, M., van As, D., Box, J. E., Charalampidis, C., Colgan, W., Fausto, R. S., Meijer, H. A. J., Mosley-Thompson, E., and van de Wal, R. S. W.: Greenland meltwater storage in firn limited by near-surface ice formation, Nature Climate Change, 6, 390–393, https://doi.org/10.1038/nclimate2899, 2016.

McConnell, J. R., Lamorey, G., Hanna, E., Mosley-Thompson, E., Bales, R. C., Belle-Oudry, D., and Kyne, J. D.: Annual net snow accumulation over southern Greenland from 1975 to 1998, Journal of Geophysical Research: Atmospheres, 106, 33 827–33 837, https://doi.org/10.1029/2001JD900129, 2001.

Medley, B., Joughin, I., Das, S. B., Steig, E. J., Conway, H., Gogineni, S., Criscitiello, A. S., McConnell, J. R., Smith, B. E., van den Broeke, M. R., Lenaerts, J. T. M., Bromwich, D. H., and Nicolas, J. P.: Airborne-radar and ice-core observations of annual snow accumulation over Thwaites Glacier, West Antarctica confirm the spatiotemporal variability of global and regional atmospheric models, Geophysical Research Letters, 40, 3649–3654, https://doi.org/10.1002/grl.50706, 2013.

Miege, C., R. Forster, R., E. Box, J., W. Burgess, E., R. McConnell, J., R. Pasteris, D., and B. Spikes, V.: SE Greenland snow accumulation rates from GPR and 3 firn cores, https://doi.org/10.18739/A2ST7DX47, 2014.

Miller, H. and Schwager, M.: Accumulation rate and stable oxygen isotope ratios of ice core ngt14C93.2 from the North Greenland Traverse, PANGAEA, p. N/A, https://doi.org/10.1594/PANGAEA.57158, 2000a.

Miller, H. and Schwager, M.: Accumulation rate and stable oxygen isotope ratios of ice core ngt27C94.2 from the North Greenland Traverse, PANGAEA, https://doi.org/10.1594/PANGAEA.57291, 2000b.

Miller, H. and Schwager, M.: Accumulation rate and stable oxygen isotope ratios of ice core ngt37C95.2 from the North Greenland Traverse, PANGAEA, https://doi.org/10.1594/PANGAEA.57297, 2000c.

Miller, H. and Schwager, M.: Accumulation rate and stable oxygen isotope ratios of ice core ngt42C95.2 from the North Greenland Traverse, PANGAEA, https://doi.org/10.1594/PANGAEA.57654, 2000d.

Miège, C., Forster, R. R., Box, J. E., Burgess, E. W., Mcconnell, J. R., Pasteris, D. R., and Spikes, V. B.: Southeast Greenland high accumulation rates derived from firn cores and ground-penetrating radar, Annals of Glaciology, 54, 322–332, https://doi.org/10.3189/2013AoG63A358, publisher: Cambridge University Press, 2013.

Montgomery, L., Koenig, L., Lenaerts, J. T. M., and Kuipers Munneke, P.: Accumulation rates (2009–2017) in Southeast Greenland derived from airborne snow radar and comparison with regional climate models, Annals of Glaciology, 61, 225–233, https://doi.org/10.1017/aog.2020.8, 2020.

Morice, C. P., Kennedy, J. J., Rayner, N. A., Winn, J. P., Hogan, E., Killick, R. E., Dunn, R. J. H., Osborn, T. J., Jones, P. D., and Simpson, I. R.: An Updated Assessment of Near-Surface Temperature Change From 1850: The HadCRUT5 Data Set, Journal of Geophysical Research: Atmospheres, 126, e2019JD032 361, https://doi.org/10.1029/2019JD032361, 2021.

Mosley-Thompson, E., McConnell, J. R., Bales, R. C., Li, Z., Lin, P.-N., Steffen, K., Thompson, L. G., Edwards, R., and Bathke, D.: Local to regional-scale variability of annual net accumulation on the Greenland ice sheet from PARCA cores, Journal of Geophysical Research: Atmospheres, 106, 33 839–33 851, https://doi.org/10.1029/2001JD900067, 2001.

Mouginot, J., Rignot, E., Bjørk, A. A., van den Broeke, M., Millan, R., Morlighem, M., Noël, B., Scheuchl, B., and Wood, M.: Forty-six years of Greenland Ice Sheet mass balance from 1972 to 2018, Proceedings of the National Academy of Sciences, 116, 9239–9244, https://doi.org/10.1073/pnas.1904242116, 2019.

Nicola, L., Notz, D., and Winkelmann, R.: Revisiting temperature sensitivity: how does Antarctic precipitation change with temperature?, The Cryosphere, 17, 2563–2583, https://doi.org/10.5194/tc-17-2563-2023, 2023.

Niwano, M., Yamaguchi, S., Yamasaki, T., and Aoki, T.: Near-surface snow physics data from SIGMA-Traverse 2018, Arctic Data archive System (ADS), Japan, N/A, N/A, https://doi.org/10.17592/001.2020091101, 2020.

Noël, B., Van De Berg, W. J., Lhermitte, S., Wouters, B., Schaffer, N., and Van Den Broeke, M. R.: Six Decades of Glacial Mass Loss in the Canadian Arctic Archipelago, Journal of Geophysical Research: Earth Surface, 123, 1430–1449, https://doi.org/10.1029/2017JF004304, 2018.

Ohmura, A. and Reeh, N.: New precipitation and accumulation maps for Greenland, Journal of Glaciology, 37, 140–148, https://doi.org/10.3189/S0022143000042891, 1991.

Ohmura, A., Calanca, P., Wild, M., and Anklin, M.: Precipitation, accumulation and mass balance of the Greenland ice sheet, Zeitschrift fur Gletscherkunde und Glazialgeologie, 35, 1–20, https://cir.nii.ac.jp/crid/1573668925528684544, 1999.

Osman, M. B., Coats, S., Das, S. B., McConnell, J. R., and Chellman, N.: North Atlantic jet stream projections in the context of the past 1,250 years, Proceedings of the National Academy of Sciences, 118, https://doi.org/10.1073/pnas.2104105118, 2021.

Otosaka, I. N., Shepherd, A., Ivins, E. R., Schlegel, N.-J., Amory, C., van den Broeke, M. R., Horwath, M., Joughin, I., King, M. D., Krinner, G., Nowicki, S., Payne, A. J., Rignot, E., Scambos, T., Simon, K. M., Smith, B. E., Sørensen, L. S., Velicogna, I., Whitehouse, P. L., A, G., Agosta, C., Ahlstrøm, A. P., Blazquez, A., Colgan, W., Engdahl, M. E., Fettweis, X., Forsberg, R., Gallée, H., Gardner, A., Gilbert, L., Gourmelen, N., Groh, A., Gunter, B. C., Harig, C., Helm, V., Khan, S. A., Kittel, C., Konrad, H., Langen, P. L., Lecavalier, B. S., Liang, C.-C., Loomis, B. D., McMillan, M., Melini, D., Mernild, S. H., Mottram, R., Mouginot, J., Nilsson, J., Noël, B., Pattle, M. E., Peltier, W. R., Pie, N., Roca, M., Sasgen, I., Save, H. V., Seo, K.-W., Scheuchl, B., Schrama, E. J. O., Schröder, L., Simonsen, S. B., Slater, T., Spada, G., Sutterley, T. C., Vishwakarma, B. D., van Wessem, J. M., Wiese, D., van der Wal, W., and Wouters, B.: Mass balance of the Greenland and Antarctic ice sheets from 1992 to 2020, Earth System Science Data, 15, 1597–1616, https://doi.org/10.5194/essd-15-1597-2023, 2023.

Ridder, K. D. and Schayes, G.: The IAGL Land Surface Model, Journal of Applied Meteorology and Climatology, 36, 167–182, https://doi.org/10.1175/1520-0450(1997)036<0167:TILSM>2.0.CO;2, publisher: American Meteorological Society Section: Journal of Applied Meteorology and Climatology, 1997.

Robin, G. D. Q., Evans, S., and Bailey, J. T.: Interpretation of Radio Echo Sounding in Polar Ice Sheets, Philosophical Transactions of the Royal Society of London. Series A, Mathematical and Physical Sciences, 265, 437–505, https://www.jstor.org/stable/73767, 1969.

Robinson, A., Calov, R., and Ganopolski, A.: Multistability and critical thresholds of the Greenland ice sheet, Nature Climate Change, 2, 429–432, https://doi.org/10.1038/nclimate1449, 2012.

Roeckner, E., Bäuml, G., Bonaventura, L., Brokopf, R., Esch, M., Giorgetta, M., Hagemann, S., Kirchner, I., Kornblueh, L., Manzini, E., Rhodin, A., Schlese, U., Schulzweida, U., and Tompkins, A.: The atmospheric general circulation model ECHAM 5. PART I: Model description, https://doi.org/10.17617/2.995269, 2003.

Rohde, R. A. and Hausfather, Z.: The Berkeley Earth Land/Ocean Temperature Record, Earth System Science Data, 12, 3469–3479, https://doi.org/10.5194/essd-12-3469-2020, publisher: Copernicus GmbH, 2020.

Ryan, J. C., Smith, L. C., Wu, M., Cooley, S. W., Miège, C., Montgomery, L. N., Koenig, L. S., Fettweis, X., Noel, B. P. Y., and van den Broeke, M. R.: Evaluation of CloudSat's Cloud-Profiling Radar for Mapping Snowfall Rates Across the Greenland Ice Sheet, Journal of Geophysical Research: Atmospheres, 125, e2019JD031 411, https://doi.org/10.1029/2019JD031411, _eprint: https://agupubs.onlinelibrary.wiley.com/doi/pdf/10.1029/2019JD031411, 2020.

Sandberg Sørensen, L., Simonsen, S. B., Forsberg, R., Khvorostovsky, K., Meister, R., and Engdahl, M. E.: 25 years of elevation changes of the Greenland Ice Sheet from ERS, Envisat, and CryoSat-2 radar altimetry, Earth and Planetary Science Letters, 495, 234–241, https://doi.org/10.1016/j.epsl.2018.05.015, 2018.

Schaller, C. F., Freitag, J., Kipfstuhl, S., Laepple, T., Steen-Larsen, H. C., and Eisen, O.: A representative density profile of the North Greenland snowpack, The Cryosphere, 10, 1991–2002, https://doi.org/10.5194/tc-10-1991-2016, 2016.

Schmidt, L. S., Schuler, T. V., Thomas, E. E., and Westermann, S.: Meltwater runoff and glacier mass balance in the high Arctic: 1991–2022 simulations for Svalbard, The Cryosphere, 17, 2941–2963, https://doi.org/10.5194/tc-17-2941-2023, 2023.

Schyberg, H., Yang, X., Køltzow, M. A. , Amstrup, B., Bakketun, , Bazile, E., Bojarova, J., Box, J. E., Dahlgren, P., Hagelin, S., Homleid, M., Horányi, A., Høyer, J., Johansson, , Killie, M. A., Körnich, H., Le Moigne, P., Lindskog, M., Manninen, T., Nielsen Englyst, P., Nielsen, K. P., Olsson, E., Palmason, B., Peralta Aros, C., Randriamampianina, R., Samuelsson, P., Stappers, R., Støylen, E., Thorsteinsson, S., Valkonen, T., and Wang, Z. Q.: Arctic regional reanalysis on single levels from 1991 to present, https://doi.org/10.24381/cds.713858f6, 2020.

Shepherd, A., Ivins, E. R., A, G., Barletta, V. R., Bentley, M. J., Bettadpur, S., Briggs, K. H., Bromwich, D. H., Forsberg, R., Galin, N., Horwath, M., Jacobs, S., Joughin, I., King, M. A., Lenaerts, J. T. M., Li, J., Ligtenberg, S. R. M., Luckman, A., Luthcke, S. B., McMillan, M., Meister, R., Milne, G., Mouginot, J., Muir, A., Nicolas, J. P., Paden, J., Payne, A. J., Pritchard, H., Rignot, E., Rott, H., Sørensen, L. S., Scambos, T. A., Scheuchl, B., Schrama, E. J. O., Smith, B., Sundal, A. V., van Angelen, J. H., van de Berg, W. J., van den Broeke, M. R., Vaughan, D. G., Velicogna, I., Wahr, J., Whitehouse, P. L., Wingham, D. J., Yi, D., Young, D., and Zwally, H. J.: A Reconciled Estimate of Ice-Sheet Mass Balance, Science, 338, 1183–1189, https://doi.org/10.1126/science.1228102, 2012.

Simmons, A. J. and Gibson, J. K.: ERA-40 Project Report Series No., 2000.

Steig, E. J., Mayewski, P. A., Dixon, D. A., Kaspari, S. D., Frey, M. M., Schneider, D. P., Arcone, S. A., Hamilton, G. S., Spikes, V. B., Albert, M., Meese, D., Gow, A. J., Shuman, C. A., White, J. W. C., Sneed, S., Flaherty, J., and Wumkes, M.: High-resolution ice cores from US ITASE (West Antarctica): development and validation of chronologies and determination of precision and accuracy, Annals of Glaciology, 41, 77–84, https://doi.org/10.3189/172756405781813311, 2005.

The IMBIE Team: Mass balance of the Greenland Ice Sheet from 1992 to 2018, Nature, 579, 233–239, https://doi.org/10.1038/s41586-019-1855-2, 2020.

Undén, P., Rontu, L., Jarvinen, H., Lynch, P., Calvo Sánchez, F. J., Cats, G., Cuxart, J., Eerola, K., Fortelius, C., García-Moya, J. A., Jones, C., Lenderink, G., McDonald, A., McGrath, R., Navascués, B., Woetman-Nielsen, N., Odegaard, V., Rodríguez Camino, E., Rummukainen, M., Room, R., Sattler, K., Hansen Sass, B., Savijärvi, H., Wichers Schreur, B., Sigg, R., Han, T., and Tijm, A.: HIRLAM-5 Scientific documentation, https://repositorio.aemet.es/handle/20.500.11765/6323, 2002.

van Dalum, C. T., van de Berg, W. J., Gadde, S. N., van Tiggelen, M., van der Drift, T., van Meijgaard, E., van Ulft, L. H., and van den Broeke, M. R.: First results of the polar regional climate model RACMO2.4, The Cryosphere, 18, 4065–4088, https://doi.org/10.5194/tc-18-4065-2024, 2024.

van den Broeke, M., Bamber, J., Ettema, J., Rignot, E., Schrama, E., van de Berg, W. J., van Meijgaard, E., Velicogna, I., and Wouters, B.: Partitioning Recent Greenland Mass Loss, Science, 326, 984–986, https://doi.org/10.1126/science.1178176, 2009.

van den Broeke, M., Box, J., Fettweis, X., Hanna, E., Noël, B., Tedesco, M., van As, D., van de Berg, W. J., and van Kampenhout, L.: Greenland Ice Sheet Surface Mass Loss: Recent Developments in Observation and Modeling, Current Climate Change Reports, 3, 345–356, https://doi.org/10.1007/s40641-017-0084-8, 2017.

van den Broeke, M. R., Enderlin, E. M., Howat, I. M., Kuipers Munneke, P., Noël, B. P. Y., van de Berg, W. J., van Meijgaard, E., and Wouters, B.: On the recent contribution of the Greenland ice sheet to sea level change, The Cryosphere, 10, 1933–1946, https://doi.org/10.5194/tc-10-1933-2016, 2016.

van der Schot, J., Abermann, J., Silva, T., Rasmussen, K., Winkler, M., Langley, K., and Schöner, W.: Seasonal snow cover indicators in coastal Greenland from in situ observations, a climate model, and reanalysis, The Cryosphere, 18, 5803–5823, https://doi.org/10.5194/tc-18-5803-2024, 2024.

Vandecrux, B., MacFerrin, M., Machguth, H., Colgan, W. T., van As, D., Heilig, A., Stevens, C. M., Charalampidis, C., Fausto, R. S., Morris, E. M., Mosley-Thompson, E., Koenig, L., Montgomery, L. N., Miège, C., Simonsen, S. B., Ingeman-Nielsen, T., and Box, J. E.: Firn data compilation reveals widespread decrease of firn air content in western Greenland, The Cryosphere, 13, 845–859, https://doi.org/10.5194/tc-13-845-2019, publisher: Copernicus GmbH, 2019.

Vandecrux, B., Box, J. E., Ahlstrøm, A. P., Andersen, S. B., Bayou, N., Colgan, W. T., Cullen, N. J., Fausto, R. S., Haas-Artho, D., Heilig, A., Houtz, D. A., How, P., Iosifescu Enescu, I., Karlsson, N. B., Kurup Buchholz, R., Mankoff, K. D., McGrath, D., Molotch, N. P., Perren, B., Revheim, M. K., Rutishauser, A., Sampson, K., Schneebeli, M., Starkweather, S., Steffen, S., Weber, J., Wright, P. J., Zwally, H. J., and Steffen, K.: The historical Greenland Climate Network (GC-Net) curated and augmented level-1 dataset, Earth System Science Data, 15, 5467–5489, https://doi.org/10.5194/essd-15-5467-2023, 2023.

Vandecrux, B., Amory, C., Ahlstrøm, A. P., Akers, P. D., Albert, M., Alley, R. B., Castro, M. A. d., Arnaud, L., Baker, I., Bales, R., Benson, C., Box, J. E., Brucker, L., Buizert, C., Chandler, D., Charalampidis, C., Cherblanc, C., Clerx, N., Colgan, W., Covi, F., Dattler, M., Denis, G., Derksen, C., Dibb, J. E., Ding, M., Dixon, D., Eisen, O., Fahrner, D., Fausto, R., Favier, V., Fernandoy, F., Freitag, J., Gerland, S., Harper, J., Hawley, R. L., Heuer, J., Hock, R., Hou, S., How, P., Humphrey, N., Hubbard, B., Iizuka, Y., Isaksson, E., Kameda, T., Karlsson, N. B., Kawakami, K., Kjær, H. A., Kreutz, K., Munneke, P. K., Lazzara, M., Lemeur, E., Lenaerts, J. T. M., Lewis, G., Lindau, F. G. L., Lindsey-Clark, J., MacFerrin, M., Machguth, H., Magand, O., Mankoff, K. D., Marquetto, L., Martinerie, P., McConnell, J. R., Medley, B., Miège, C., Miles, K. E., Miller, O., Miller, H., Montgomery, L., Morris, E., Mosley-Thompson, E., Mulvaney, R., Niwano, M., Oerter, H., Osterberg, E., Otosaka, I., Picard, G., Polashenski, C., Reijmer, C., Rennermalm, A., Rutishauser, A., Scanlan, K., Simoes, J. C., Simonsen, S. B., Smeets, P. C. J. P., Smith, A., Solgaard, A., Spencer, M., Steen-Larsen, H. C., Stevens, C. M., Sugiyama, S., Svensson, J., Tedesco, M., Thomas, E., Thompson-Munson, M., Tsutaki, S., As, D. v., Broeke, M. R. V. d., Tiggelen, M. v., Wang, Y., Wilhelms, F., Winstrup, M., Xiao, J., and Xiao, C.: The SUMup collaborative database: Surface mass balance, subsurface temperature and density measurements from the Greenland and Antarctic ice sheets (2024 release), https://arcticdata.io/catalog/view/doi%3A10.18739%2FA2M61BR5M, 2024.

Velicogna, I., Sutterley, T. C., and van den Broeke, M. R.: Regional acceleration in ice mass loss from Greenland and Antarctica using GRACE time-variable gravity data, Geophysical Research Letters, 41, 8130–8137, https://doi.org/10.1002/2014GL061052, 2014.

Vernon, C. L., Bamber, J. L., Box, J. E., van den Broeke, M. R., Fettweis, X., Hanna, E., and Huybrechts, P.: Surface mass balance model intercomparison for the Greenland ice sheet, The Cryosphere, 7, 599–614, https://doi.org/10.5194/tc-7-599-2013, 2013.

Vinther, B. M., Freitag, J., Kipfstuhl, S., Weißbach, S., Karlsson, N. B., Münch, T., and Hörhold, M.: Accumulation rate of the B26_2011 firn core, PANGAEA, https://doi.org/10.1594/PANGAEA.945666, 2022.

Virtanen, P., Gommers, R., Oliphant, T. E., Haberland, M., Reddy, T., Cournapeau, D., Burovski, E., Peterson, P., Weckesser, W., Bright, J., van der Walt, S. J., Brett, M., Wilson, J., Millman, K. J., Mayorov, N., Nelson, A. R. J., Jones, E., Kern, R., Larson, E., Carey, C. J., Polat, , Feng, Y., Moore, E. W., VanderPlas, J., Laxalde, D., Perktold, J., Cimrman, R., Henriksen, I., Quintero, E. A., Harris, C. R., Archibald, A. M., Ribeiro, A. H., Pedregosa, F., and van Mulbregt, P.: SciPy 1.0: fundamental algorithms for scientific computing in Python, Nature Methods, 17, 261–272, https://doi.org/10.1038/s41592-019-0686-2, 2020.

Yang, X., Schyberg, H., Palmason, B., Bojarova, J., Box, J. E., Pagh Nielsen, K., Amstrup, B., Peralta, C., Høyer, J., Nielsen Englyst, P., Homleid, M., Køltzow, M. A. , Randriamampianina, R., Dahlgren, P., Støylen, E., Valkonen, T., Thorsteinsson, S., Körnich, H., Lindskog, M., and Mankoff, K.: C3S arctic regional reanalysis — full system documentation, Tech. rep., Copernicus Climate Change Service (C3S), ECMWF, https://confluence.ecmwf.int/display/CKB/Copernicus+Arctic+Regional+Reanalysis+%28CARRA%29%3A+Full+system+documentation, 2020.